Stony Brook University

Post-Seismic Strain and Stress Evolution from Continuous GPS Observations

A Thesis Presented

by

Gina Nicole Shcherbenko

to

The Graduate School

in Partial Fulfillment of the

Requirements

for the Degree of

Master of Science

in

Geosciences

Stony Brook University

August 2014

Stony Brook University

The Graduate School

Gina Nicole Shcherbenko

We, the thesis committee for the above candidate for the

Master of Science degree, hereby recommend

acceptance of this thesis.

Dr. William E. Holt – Thesis Advisor
Professor, Geosciences

Dr. Daniel M. Davis – Committee Chairperson
Professor and Chair, Geosciences

Dr. Christiane Stidham – Second Reader
Lecturer, Geosciences

This thesis is accepted by the Graduate School

Charles Taber
Dean of the Graduate School

Abstract of the Thesis

Post-Seismic Strain and Stress Evolution from Continuous GPS Observations

by

Gina Nicole Shcherbenko

Master of Science

in

Geosciences

Stony Brook University

2014

Strain evolution and stress evolution following the 4 April 2010 M7.2 El Mayor-Cucapah earthquake are modeled using an adaptation of the strain transient detection tool developed by *Holt and* Shcherbenko 2013. The evolution of stress is calculated from postseismic strains, which are modeled from continuous GPS horizontal displacements. Strain fields are modeled in 2 ways; the total strain field based on total observed cGPS displacements, and the residual strain field, which subtracts a reference field from the total model. The residual shows anomalous strains resulting from the postseismic relaxation of the 2010 event. Anomalous and total strains are modeled in 0.1 year epochs for 2.4 years following the event. Both total and anomalous strains are converted into stress changes over time, assuming elastic incompressible behavior. Following the El Mayor event, the GPS constrained strain evolution shows the following: (1) The Southern San Andreas experiences a reduced rate of right-lateral strike slip strain accumulation between 3 July 2010 and 7 August 2012 (Figure 16a-d). (2) The San Jacinto Fault

has normal rate of right-lateral strike-slip strain accumulation during this time. (3) Before the Brawley swarm of 26 August 2012, the state of strain evolves to enable unclamping of a left-lateral fault zone in the Brawley Seismic Zone (Figure 16a-d). (4) Large shear strains accumulate on the Laguna Salada Fault (northernmost segment)/southern Elsinore FZ (Figure 16a-d). We converted the strain changes into Coulomb stress changes on existing faults (both right-lateral and left-lateral). Several regions show increased Coulomb stress changes throughout the postseismic process. Furthermore, the Coulomb stress changes on the faults in the region progressively increase toward failure up to the time of the Brawley swarm (Figures 30, 31, 32, 33).

This thesis is dedicated to my family and friends,

my constant reminders of how fortunate I am.

Table of Contents

List of Figures

Figure Page

Figure Page

Figure Page

Figure Page

Figure Page

Acknowledgments

I would first like to thank my advisor, Dr. Bill Holt, for his patience and guidance. You provided me with the best opportunity I have ever had, and I am a better scientist because of you. Performing this research has been an honor; I am grateful to have been able to do it, as well as attend conferences to share my work with and learn from others.

I would also like to thank Dr. Dan Davis, for our many helpful and fun chats about life, grad school, geology and astronomy. It was a pleasure to be your Teaching Assistant, and I sincerely appreciate your mentorship.

The support of the Professors in the Geosciences Department at Stony Brook University has been immeasurable. Thank you for sharing your wisdom and guidance with me, and always being available for help. I would like to acknowledge Dr. Christiane Stidham for being on my Graduate Committee, as well as Dr. Matt Whitaker for helping me find my voice.

Kara Dias and Ashley Thompson have been the best pair of friends I could hope to have. Thanks for being there with me through the twists and turns of Grad School. I would also like to acknowledge my labmates, and give a special thanks to Yuanyuan Liu and Attreyee Ghosh for all of your help.

Finally, I'd like to thank my wonderful family, my Mom, Dad, Stepmom, Stepdad, Grandma, Grandpa, Mike, Diana and Ernie. Thank you for supporting my fascination with geology, putting up with the endless rock collection, and listening to my relentless raving about the earth.

The Plate Boundary Observatory GPS data are based on services provided by the UNAVCO Facility with support from the National Science Foundation (NSF) and National Aeronautics and Space Administration (NASA) under NSF Cooperative Agreement No. EAR-0735156. This work was supported by SCEC award# 12036 and NSF-EAR-1052989.

Chapter 1: Introduction

In this thesis I provide an overview of the strain transient detection tool developed by *Holt and Shcherbenko* (2013) and use it to analyze transient deformation following the El Mayor-Cucapah earthquake. This transient tool can be adapted and used to analyze anomalous strain wherever a dense cGPS (continuous Global Positioning System) network exists. In addition to retrospective strain detection, this tool can be used to better understand the evolution of strain transients over varying time epochs. Strain anomalies with or without a known cause can be quantified, analyzed, and used to calculate stress changes. A better understanding of stress evolution can provide valuable insight into fault mechanics, seismicity rate changes, and the earthquake cycle in general.

Chapter 2 is a publication that provides the background and initial motivations behind the strain transient detection work. William Holt and I published it in May 2013 in Seismological Research Letters. I performed the retrospective analyses described in section 5.0 of Chapter 2. I made the figures of the time series, as well as any maps used in the PBO data analyses, in Chapter 2. In Chapter 3 I describe an adaptation of the strain transient detection tool from Chapter 2, which is used to investigate postseismic deformation and strain associated with the 2010 M7.2 El Mayor-Cucapah earthquake, particularly along major faults in that region (Appendix A). In Chapter 4 I provide the results of Coulomb stress changes derived from the postseismic strains described in Chapter 3, and I discuss the changes in the state of stress that may arise from this large earthquake. In Chapter 5 I summarize the conclusions from the transient analysis and describe the potential for future work based on the methods of Chapters 2, 3 and 4.

Chapter 2: Toward a Continuous Monitoring of the Horizontal Displacement Gradient Tensor Field in Southern California using cGPS Observations from PBO

2.1 - Introduction

Detection and characterization of strain transients provides opportunities for a better understanding of crust and mantle rheology [*Freed and Burgman*, 2004; *Freed et al*., 2007; *Pollitz et al*., 2012], fault zone behavior [*McGuire and Segall*, 2003; *Myazaki et al.*, 2011], and the mechanics of parts of the earthquake cycle [*Dragert and Wang*, 2011; *Bartlow et al*., 2011]. The relatively dense coverage of continuous GPS (cGPS) within western North America, through EarthScope Plate Boundary Observatory (PBO), enables the possibility of detecting crustal strain transient phenomenon on a variety of spatial and temporal scales [*Ohtani et al*., 2010; *Ji and Herring*, 2011]. In this chapter we present a geodetic network-processing tool for detection of anomalous strain transients in Southern California, or within any region with reasonably dense cGPS coverage. The modeling procedure determines time-dependent displacement gradient fields from cGPS time series [*Hernandez et al*., 2005, 2007] and determines the significance of any departures of this field relative to a geodetic reference model. The derived field satisfies strain rate compatibility relations everywhere within the plate boundary zone on a sphere. Given sufficient spatial coverage of cGPS, the method can detect anomalous strain, either from shear or volume sources, and either on or off of the known faults.

In section 2.2 we present a brief description of the derivation of the geodetic reference model. We show from a benchmarking exercise that GPS observations in southern California [*Shen et al*., 2011] are sufficiently dense to provide a reliable estimate of a reference model. In section 2.3 we introduce the method for interpolating the individual cGPS time series for time-

dependent estimates of displacement, followed by a description of the analysis of all displacements for the time-dependent horizontal displacement gradient tensor field. In section 2.4 we present examples of a blind test, where synthetic transients, generated using *Fakenet* [*Agnew*, 2013, Accepted, SRL], were detected using our network-processing tool. In section 2.5 we present results obtained to date from analysis of cGPS observations within the PBO network. Implications for future work are provided in the Discussion and Conclusions (Section 2.6).

2.2 - Determination of a Geodetic Reference Model

The method presented in this paper determines whether a strain field derived from the cGPS observations differs significantly from that predicted by a geodetic reference model. The reference model (strains and rotations) is obtained from the interpolation of the SCEC4.0 GPS velocity field [*Shen et al*., 2011] using the method of *Beavan and Haines* [2001]. This same methodology is used to also interpolate the time dependent estimates of displacement, with some differences explained in section 3.0. Regularization of the solution for Southern California consists of obtaining the sharpest estimate of strain tensor field possible that can be supported by the GPS data. The smoothing of the strain solution is controlled through optimization of the following functional in a formal least-squares joint inversion of strain and displacement observations:

$$\chi = \sum_{cells} \sum_{ij,kl} (\hat{e}_{ij} - e_{ij}^{obs})^T \mathbf{V}_{ij,kl}^{-1} (\hat{e}_{kl} - e_{kl}^{obs}) + \sum_{knots} \sum_{i,j} (\hat{u}_i - u_i^{obs})^T \mathbf{V}_{i,j}^{-1} (\hat{u}_j - u_j^{obs}), \quad (1)$$

where $\mathbf{V}_{ij,kl}$ is the variance-covariance matrix of the strains, $\mathbf{V}_{i,j}$ is the variance-covariance of the displacements, $\hat{e}_{ij}$ and e_{ij}^{obs} are the model and observed strains, and $\hat{u}_i$ and u_i^{obs} are the model and observed displacements. The fitting algorithm that minimizes (1) is equivalent to a finite element

method that satisfies force balance equations (spherical Earth). The methodology solves the Weak formulation of the linear problem, where the basis functions for the displacement rates at any time snap shot are higher order elements involving the Bessel form of bi-cubic spline interpolation on a generally curvilinear grid of quadrilateral sub-domains [*de Boor*, 1978; *Beavan and Haines*, 2001] (0.1°x0.1° grid, Figure 1). The final model predicts a continuous velocity and strain rate tensor field (for the reference geodetic model). Finer grid spacing can be used to adapt to problems supported by dense station spacing. We use a constant Poisson's ratio of 0.25 and velocity boundary conditions may or may not be imposed. Also, *a priori* constraints from fault location, strike and expected range of fault slip rates can be used to define anisotropic and inhomogeneous components of the variance-covariance matrix $\mathbf{V}_{ij,kl}$, which influences the model parameter estimates for interpolated displacements and strains. Thus, the fitting procedure has a physics-based link to force-balance on a sphere with additional constraints provided by knowledge of structural and geodetic information. The method is similar to NeoKinema [*Bird*, 2009], but it does not have explicit fault and block locations imposed. That is, primarily the GPS velocity field dictates the features of the full horizontal velocity gradient tensor field.

In the case of fitting the SCEC4.0 velocity field, we do not use an observed strain rate field in (1). This results in a solution that matches the GPS velocities under the constraint that the model strain rate field constitutes a minimum global value of the second invariant of model strain rate. Damping or smoothing of the solution is achieved through construction of the variance-covariance matrix, $\mathbf{V}_{ij,kl}$. The structure of this variance-covariance matrix is obtained using published fault slip rate uncertainties for California (see *Shen-Tu et al*. [1999] for method of estimating strain rate variances and covariances). When fault slip rate uncertainties are used to define $\mathbf{V}_{ij,kl}$, there is directional information involved, since fault strike, dip, and rake

influence the estimates of the strain rate components. The pure strike-slip component of the total horizontal velocity gradient tensor field (for the geodetic reference model) is shown in Figure 2.

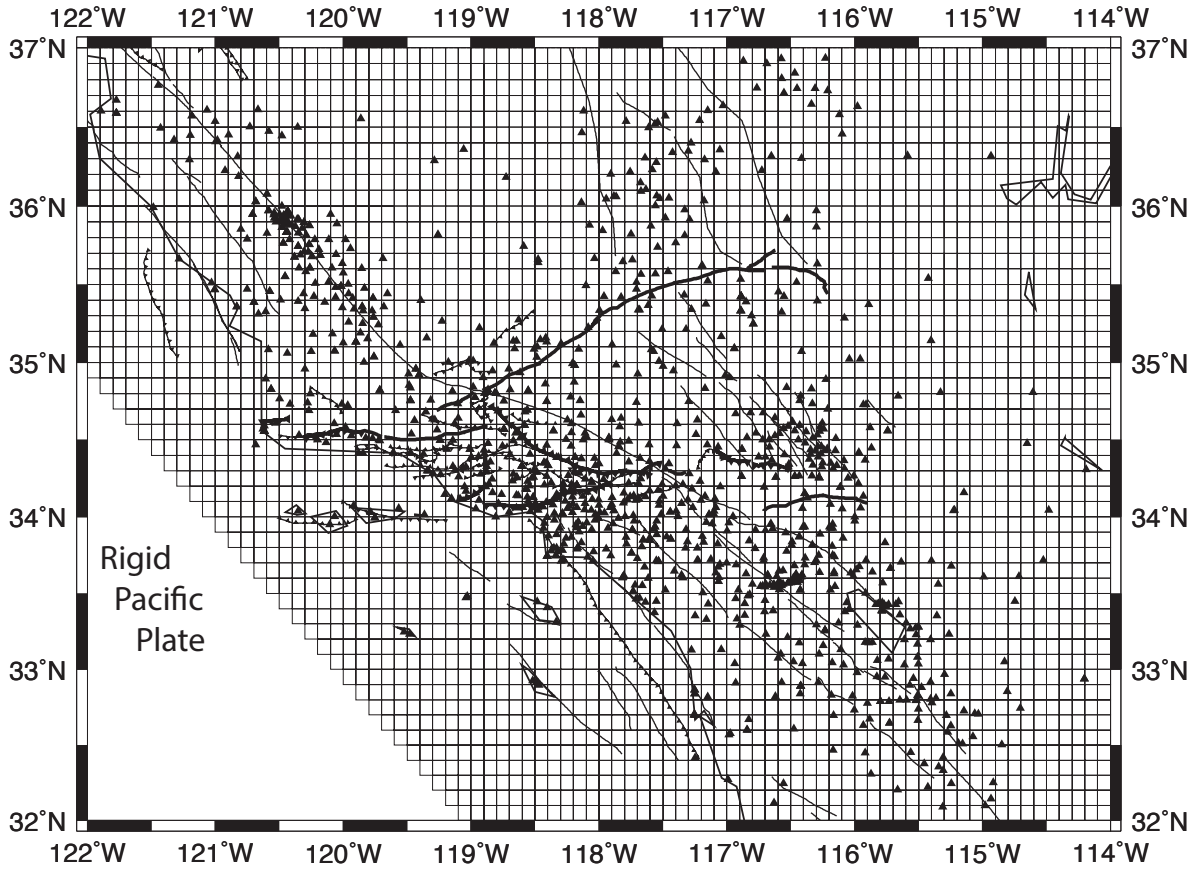

Figure 1. Grid on spherical Earth surface (0.1°x0.1°) for bi-cubic Bessel interpolation of GPS observations from SCEC4.0. Station locations are depicted as triangles.

In addition to the uncertainties in fault slip, we also use an adjustable isotropic component of strain rate variance, embedded in $\mathbf{V}_{ij,kl}$, as a measure of the variance associated with unknown or unmapped deformation. This isotropic component of variance is adjusted until the reduced Chi-Squared misfit to the GPS velocities is optimal (around 1.0). In the case of fitting the time-dependent displacements (discussed in section 2.3), the isotropic component

represents the possibility of a departure from the expected strain, associated with a transient event.

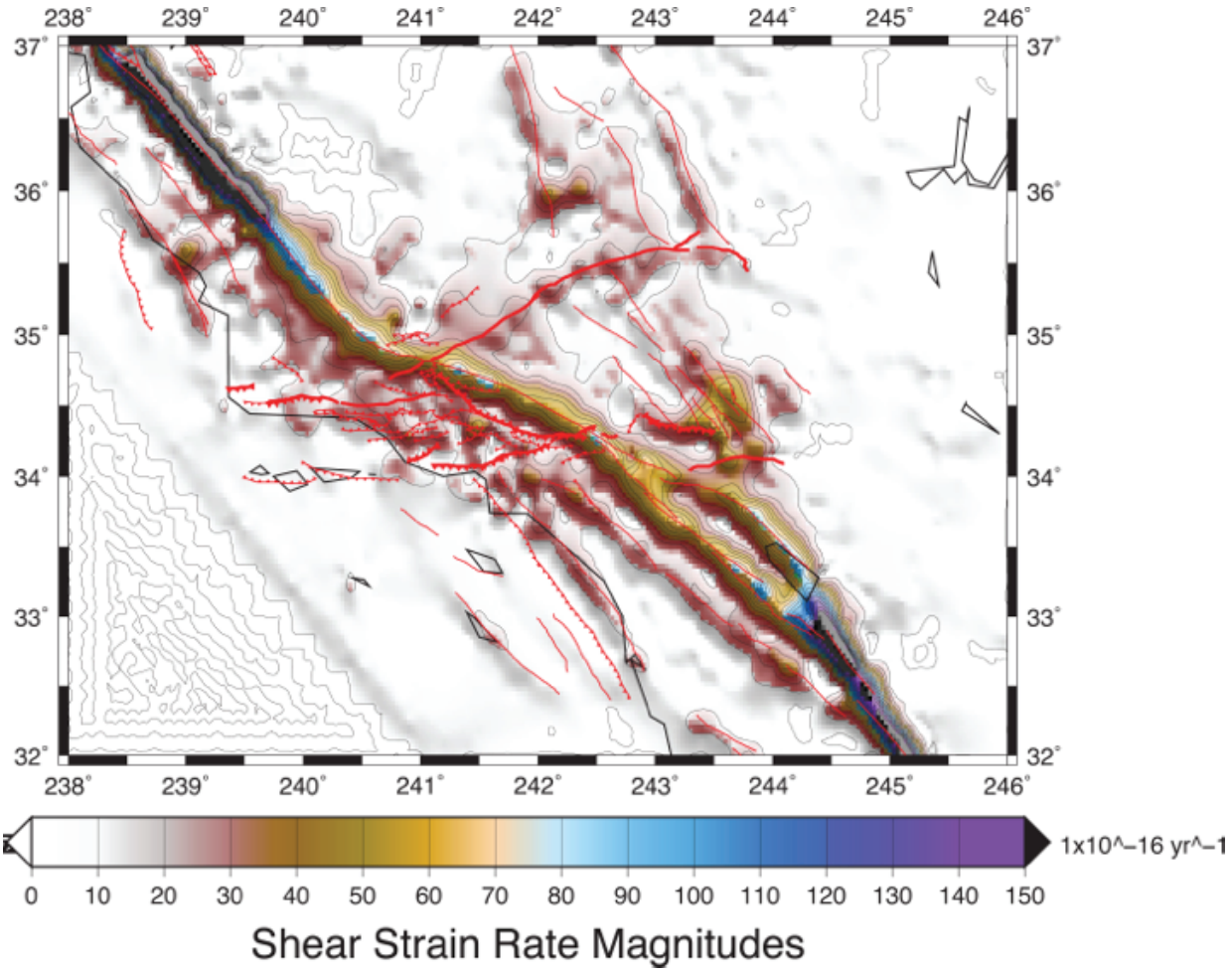

Figure 2. Shear strain rates (associated with pure strike-slip style deformation) obtained from inversion of the SCEC4.0 GPS data set [*Shen et al*., 2011] using treatment of *Beavan and Haines* [2001]. The total solution, which contains shear, dilatation, and rotation, is used as the geodetic reference field.

In all of our previous work we have used an anisotropic variance-covariance structure for strain rates. As interpolation of GPS can hold some problems of non-uniqueness, this variance-covariance structure imposes an influence on the solution such that interpolated GPS more closely complies with the expected styles of deformation, while also satisfying strain rate compatibility. *Baxter et al*. [2011] showed that significant strain rate artifacts (dilatational rates)

arise from interpolation of GPS velocities with irregular station distributions (as shown in Figure 1). We therefore perform benchmarking tests using the station spacing from the SCEC4.0 velocity field.

2.2.1 - Benchmarking Results Using Output from Okada's Elastic Dislocation Routine

We generated synthetic interseismic displacement fields using the code Coulomb 3.2 [*King et al*., 1994; *Lin and Stein*, 2004], an adaptation of *Okada* (1992). We output displacements at the same station spacing as the SCEC4.0 velocity field [*Shen et al*., 2011] (Figures 1, 3). For simplification we generated displacements for a single pure strike-slip fault that passed through the approximate centroid of the GPS station density. For the benchmarking exercise only, the synthetic fault was N-S oriented. The California stations were rotated about a point at about 32° S, 115°W, such that the distribution of stations that roughly follow the NW oriented trend of the plate boundary zone are now oriented N-S. A 0.1°x0.1° grid (same grid spacing as used for Southern California – Figure 1) was used for the bi-cubic interpolation of the synthetic displacements. The fault is slipping at 25 mm/yr with a locking depth of 10 km. In this particular test case the longitude is arbitrary, and the fault was placed at a longitude of 5° (Figures 3a, b). The variances and covariances of the strain rates (see equation 1) reflect the *a priori* expectation of a strike-slip fault in the region, with unknown slip rate magnitude. The shear strain rates, obtained from the interpolation of displacements from the dislocation model, are shown in Figure 3a. Two example cross-sections [Figure 3d] show that both the theoretical shear strains [*Okada*, 1992] and the strains from interpolation are nearly identical. The dilatational strain rates from this model, which should ideally be zero, varied between

$\pm$ 0.25 x 10^{-16} s^{-1}, almost two orders of magnitude smaller than the magnitude of shear strain rate (120 x 10^{-16} s^{-1}). Therefore, the interpolation method that we employ (with anisotropic variance-covariances of strain rates) does not show the strain rate artifacts that *Baxter et al*. [2010] described and found when they interpolated the present-day GPS station distribution in southern California.

The benchmark test suggests that the distribution of GPS in the SCEC4.0 velocity field is sufficient to obtain a reliable estimate of a geodetic reference field. The reference field represents a picture of the relatively steady-state interseismic strain rate field, as the effects of most postseismic phenomenon have been removed [*Shen et al*., 2011].

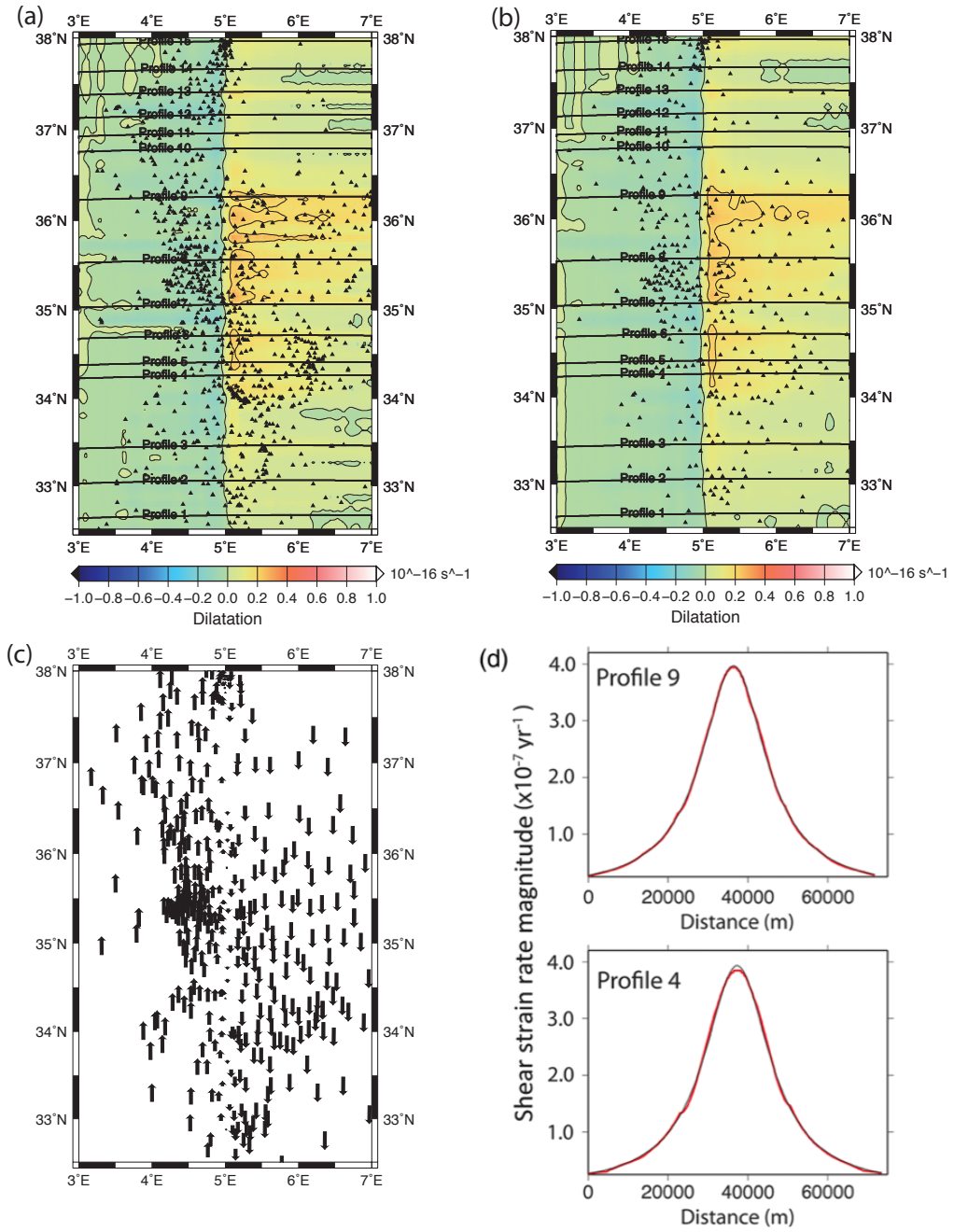

Figure 3. (**a)** Contoured dilatational strain rates from fitting of displacements (interseismic) generated from elastic dislocation model [Okada, 1992; King et al., 1994; Lin and Stein, 2004], where a locking depth of 10 km and a slip rate of 25 mm/yr were used. Triangles, displacements are output at the SCEC4.0 spacing station, rotated 51° about the point 32°S, 115°W. **(b)** Contoured dilatational strain rate from joint fitting of strain-tensor field from (a), triangles, velocities output at the PBO station distribution, rotated about the same points as in (a), and with the same fault-slip parameters as (a). (**c**) The displacement-rate field generated using an elastic dislocation model at the PBO stations. These displacement rates were interpolated on a 1°x1° grid to yield the strain solution in 3b,d (see text). **(d)** Red, profiles of shear-strain rate from interpolation; thin black line, the output shear-strain rate from the dislocation model.

2.3 - Method for Obtaining Time-Dependent Displacement Estimates from cGPS Observations

We use general polynomial functions to interpolate continuous displacement GPS time series and generate time dependent model displacements for all cGPS stations in the SCIGN network [*Hernandez et al*., 2005, 2007]. A forth order representation is:

$$d(t) = \frac{1}{24}(a)t^4 + \frac{1}{6}(b)t^3 + \frac{1}{2}(c)t^2 + (d)t + e + f\sin(\tfrac{2\pi t}{T}) + g\cos(\tfrac{2\pi t}{T}) + h\sin(\tfrac{4\pi t}{T}) + i\cos(\tfrac{4\pi t}{T}) \qquad (2)$$

A weighted least-squares inversion of each displacement time series, d(t), from the cGPS observations, provides estimates of the coefficients. Note that coefficients *f,g,h*, and *i* are for the annual and semi-annual terms. This function fits generally long-wavelength non-linear trends, but it is inadequate for capturing shorter-term transients. Once the fit to the time series is obtained with (2), the annual and semi-annual signals are then removed from the cGPS time series. A moving average filter, capable of capturing short-term variations, is then fit to the time series with seasonal estimates removed and these filtered estimates of displacement are then used in the remainder of the analysis (Figure 4). For retrospective analyses that involve a search for anomalous strain accumulation over periods greater than 2.5 months into the past, a two-week (centered) moving average has proven effective for picking up transients in the blind test exercise (section 2.4). For retrospective analyses of anomalous strain accumulation over the past 2 weeks, we use a moving average over 3 days of data. For daily analysis, no moving average is used. Instead, we simply look at the differences between the averaged daily position estimates. Moreover, the entire time history can be analyzed for anomalous strain within any chosen time frame.

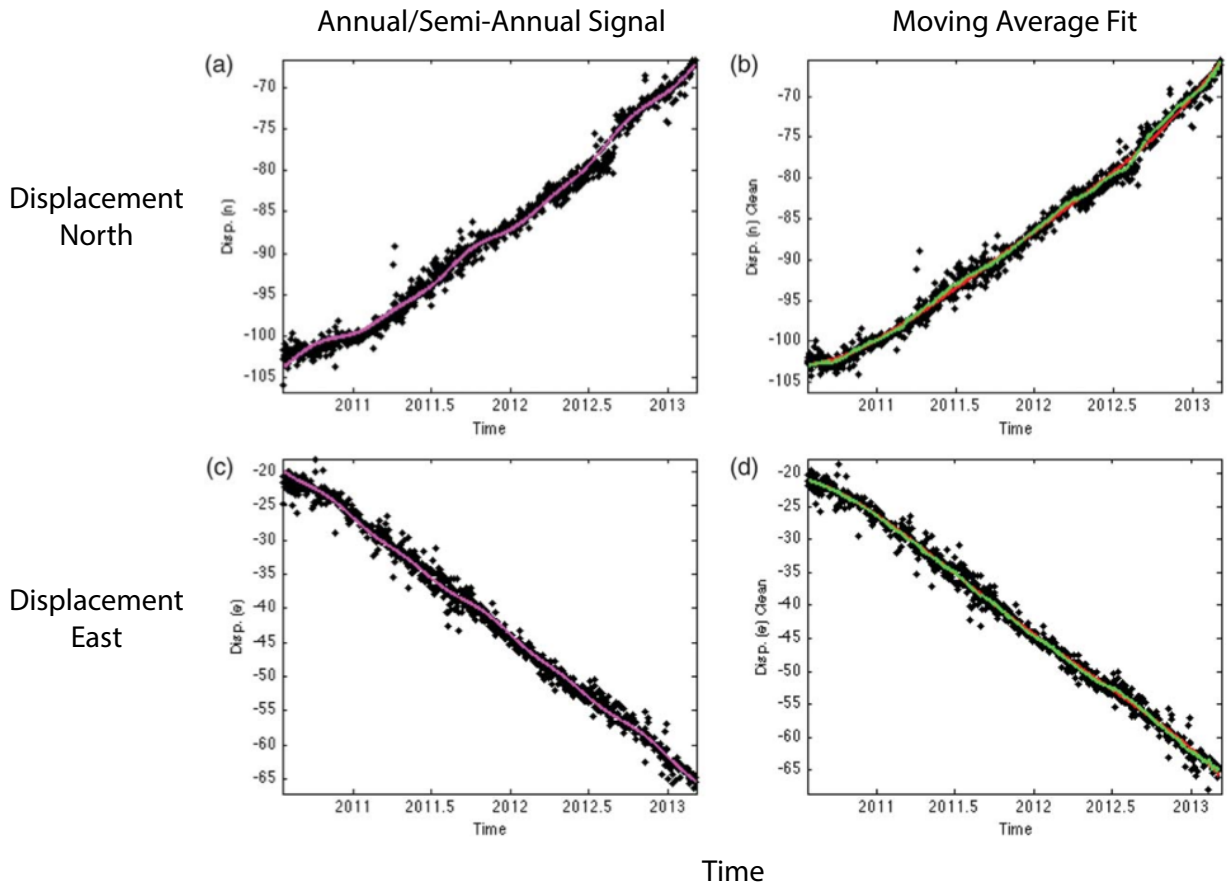

Figure 4. Time series analysis for station P507 for (**a,b**) north-south and (**c,d**) east-west displacement components, with fourth-order polynomial fit; (**a,c**) magenta line fit to black dots, annual and semiannual terms; (**b,d**) green line fit to black dots, one-month moving average (centered) fit to residual time series (annual and semiannual terms removed), and red line, the fourth-order polynomial fit to the cleaned time series.

2.3.1 - Modeling the Time Dependent Displacements for Detection of Anomalous Strain

Displacement estimates from the cGPS time series, along with their estimated standard errors, are output and modeled, using the interpolation scheme described in section 2.2. The observed strain values in (1) are now from the reference solution. This imposes the constraint that in the absence of any other information, the model solution for a given epoch will conform to that steady-state tectonic pattern. The rotation pole for the Pacific Plate, obtained from the geodetic reference solution, is used to provide a displacement boundary condition for the time-

dependent epoch solution. The isotropic component of the strain variance, embedded in $\mathbf{V}_{ij,kl}$ in (1), and constant in magnitude everywhere, represents the *a priori* expected variance associated with a potential strain transient. This component is isotropic, and constant in magnitude for all regions, because there is no prior expectation on the orientation of transient strain field. The magnitude of this one adjustable parameter is varied until the reduced chi-squared difference between model and observed displacements is close to 1.0. Once a solution is obtained for a given time epoch or interval, the reference solution is then subtracted to determine a residual. The statistical significance of the strain residual is then analyzed to determine if it constitutes a crustal strain transient.

2.3.2 - Evaluation of the Significance of the Residual Strain

Our procedure tests the null hypothesis that the time-dependent strain field inferred from the cGPS is equivalent to the long-term steady-state reference solution (Figure 1), using the t-statistic:

$$t = \frac{\hat{E} - E_o}{S_{\hat{E}-E_o}}, \tag{3}$$

where $\hat{E}$ is the average model second invariant of strain within an area, determined from the epoch solution defined by the cGPS displacements, E_o is the second invariant of strain from the reference model, and $S_{\hat{E}-E_o}$ is the standard error of the strain differences between the two models. We flag all regions that differ from the reference solution if their strains are significant at greater than the 95% confidence level (t-statistic greater than 1.96).

2.4 - Testing the Method Using the SCEC IV Transient Exercise

The synthetic cGPS time series, created using *Fakenet* [*Agnew*, 2013] from SCEC IV A, B, and C, were analyzed using the method described in section 2.3. Time series for A and B were analyzed retrospectively, whereas the time series for C was analyzed "blind", without knowledge as to the location or duration of the slow event. Anomalous strains and displacements, corresponding to the true solution, were well resolved both temporally and spatially for all three sets of time series (compare solution with true displacements in Figures 5-7).

Results from the SCEC IV transient exercise indicate that we can accurately resolve anomalous displacements and strain associated with total anomalous surface displacements of less than 1 cm, which occur over time intervals of 6 - 8 weeks. No errors were provided for the synthetic cGPS time series, but we assumed standard errors of ± 3 mm for the cGPS daily position estimates.

2.5 - Analysis of PBO Data

We perform a retrospective analysis of accumulated strain over periods lasting 24 hours, 2-weeks, 1-month, 3 months, 6 months, 1 year, and two years. These analyses can be performed each day, following an automatic download of cGPS observations from PBO. Moreover, the entire time history of the cGPS time series of PBO can be analyzed for anomalous strain within any chosen time interval. Any statistically significant strain difference is termed here a strain anomaly.

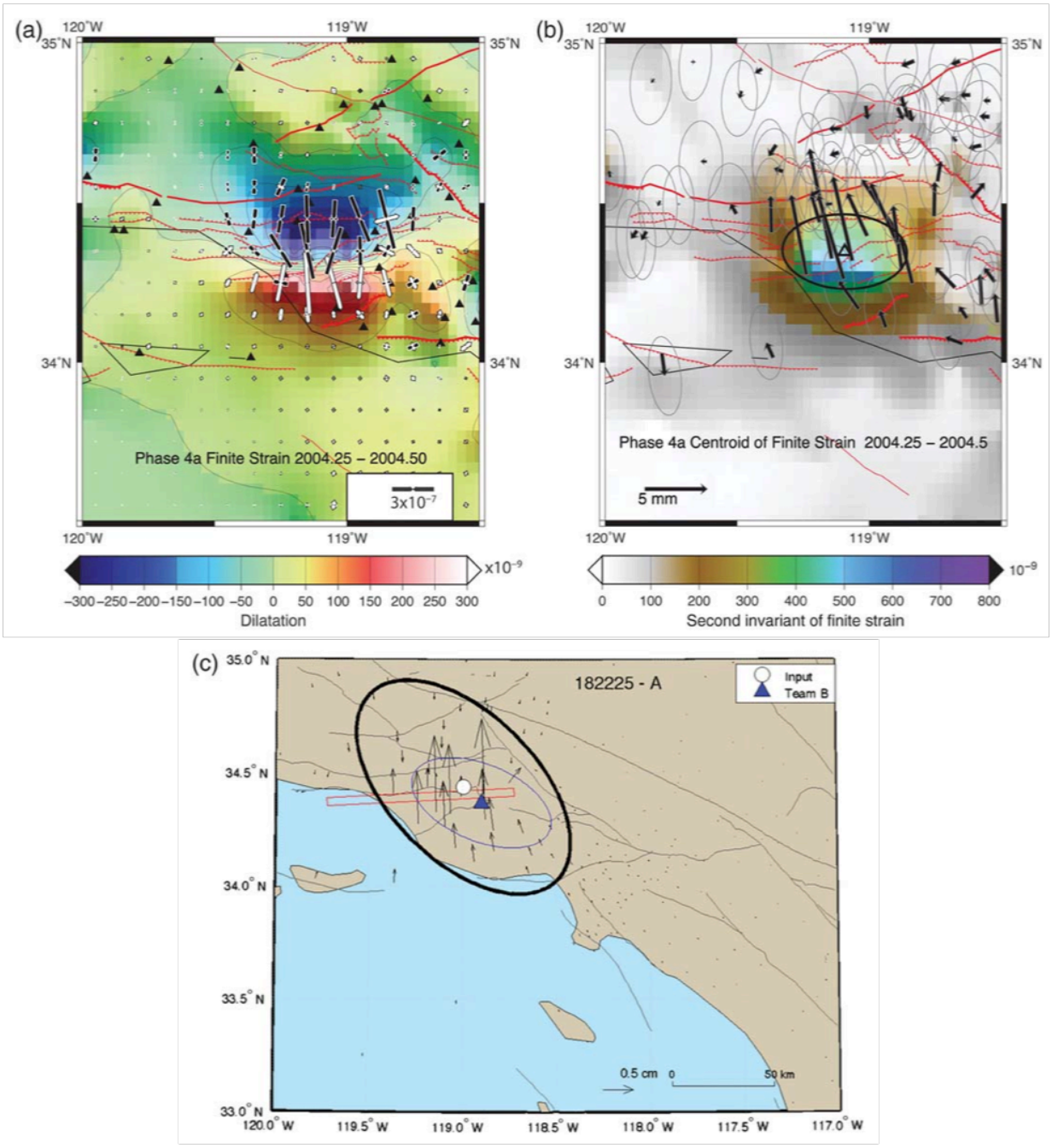

Figure 5. (**a**) Contoured dilatations, finite anomalous strain (negative, contraction; positive, extension) with principal axes of finite strain (bold, compressional; open, extensional) for IV-a. (**b**) Second invariant of anomalous finite strain and model displacements (one-sigma error ellipse) with one-sigma confidence ellipse for location of transient. (**c**) True solution input embedded in the synthetic time series for IV-a. The algorithm recovered the finite anomalous displacements and anomalous strain for this synthetic slow event (thrust) in both time and space.

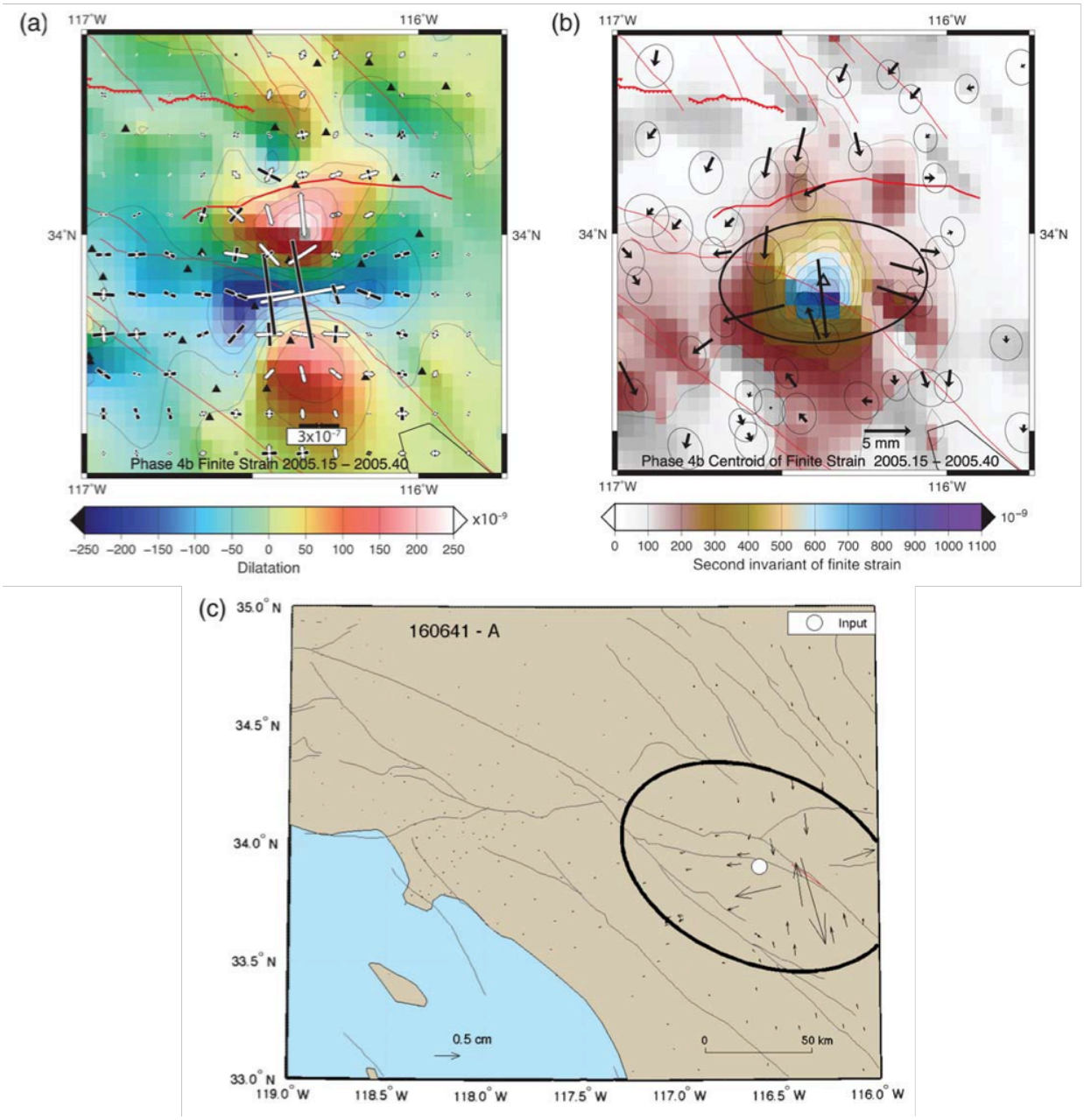

Figure 6. (**a**) Contoured dilatations, finite anomalous strain with principal axes of finite strain (bold, compressional; open, extensional) for IV-b. (**b**) Second invariant of anomalous finite strain with model finite displacements (one-sigma error ellipses) with one-sigma confidence ellipse for location of transient. (**c**) True solution input embedded in time series for IV-b. The algorithm resolved the finite anomalous displacements and anomalous strain for this synthetic slow event (strike-slip on southern San Andreas) in both time and space.

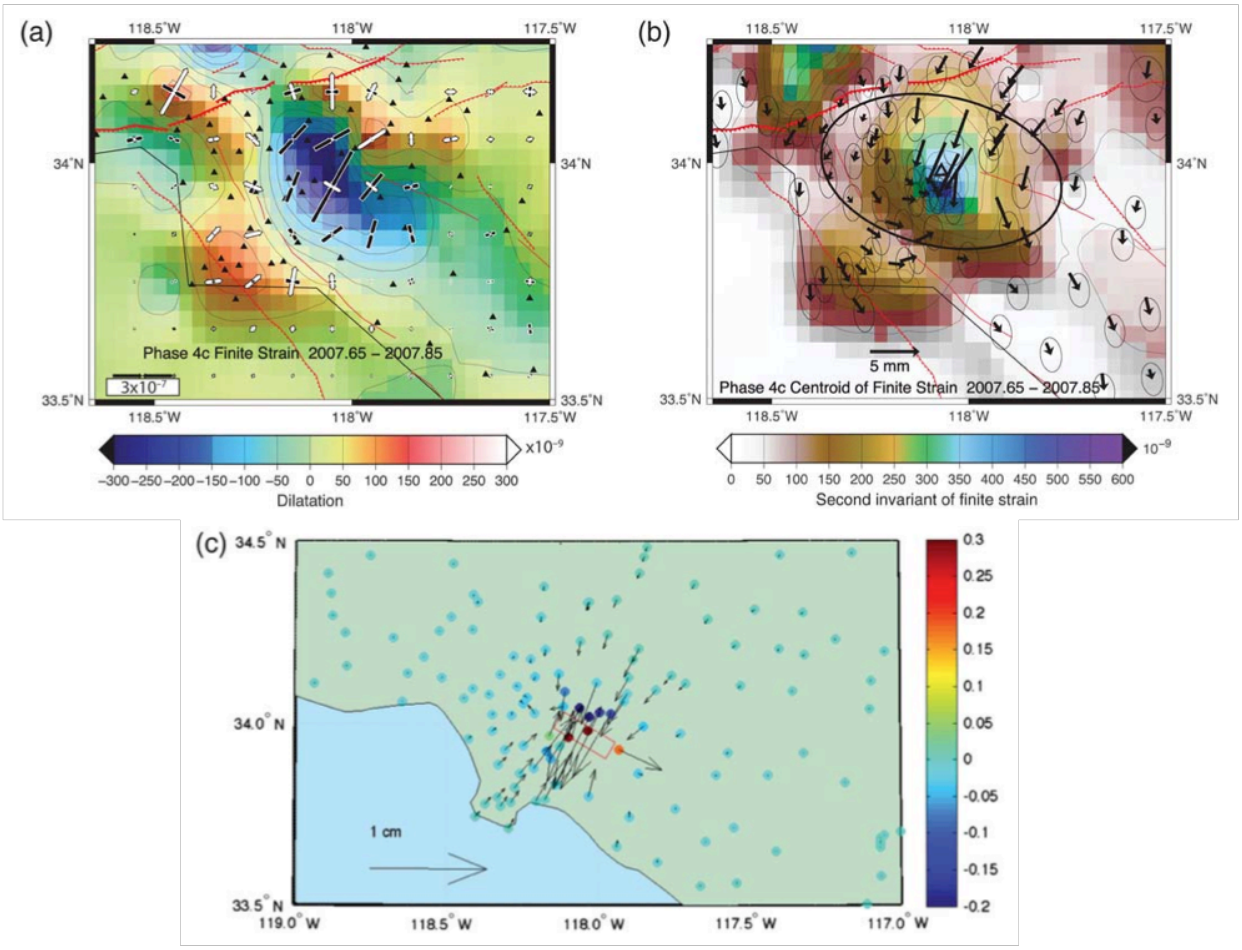

Figure 7. (**a**) Contoured dilatations, finite anomalous strain with principal axes of finite strain (bold, compressional; open, extensional) for IV-c. (**b**) Second invariant of anomalous finite strain with model displacements (one-sigma error ellipses) with one-sigma confidence ellipse for location of transient. (**c**) True solution input embedded in time series for IV-c. The algorithm recovered the finite anomalous displacements and anomalous strain for this synthetic slow event (thrust) in both time and space.

Analyses of the cGPS data from PBO have revealed recent significant strain anomalies that have accumulated on a variety of time scales (Figures 8, 9 and 10). Some of these are linked with known earthquakes (postseismic relaxation in El Mayor-Cucapah [*Pollitz et al*., 2012]; Brawley Swarm coseismic, Figure 8a), whereas others are linked with unknown, and potentially slow-slip, processes (Parkfield and San Simeon regions) (Figure 10c).

These patterns of significant anomalous accumulated strain (Figure 10) over the last two years are heterogeneous (Figures 9 and 11), are likely associated with the postseismic effects of the El Mayor-Cucapah event, and reach as far north as the Garlock fault and the Big Bend region of the San Andreas. Some of the heterogeneity may be an artifact of the station distribution, but there appears to be a trend of significant anomalous strain within the major fault zones (San Andreas), including the Hector Mine region. Moreover, results show that many of these fault zones experienced a strain change that would be consistent with a reduced rate of strain accumulation on the structures following El Mayor-Cucapah (compressional axes of principal strain oriented east-northeast-west-southwest). A few regions, however, experienced a strain change that constitutes a potential increase in strain accumulation. There are also significant rotations associated with these anomalies (Figure 9).

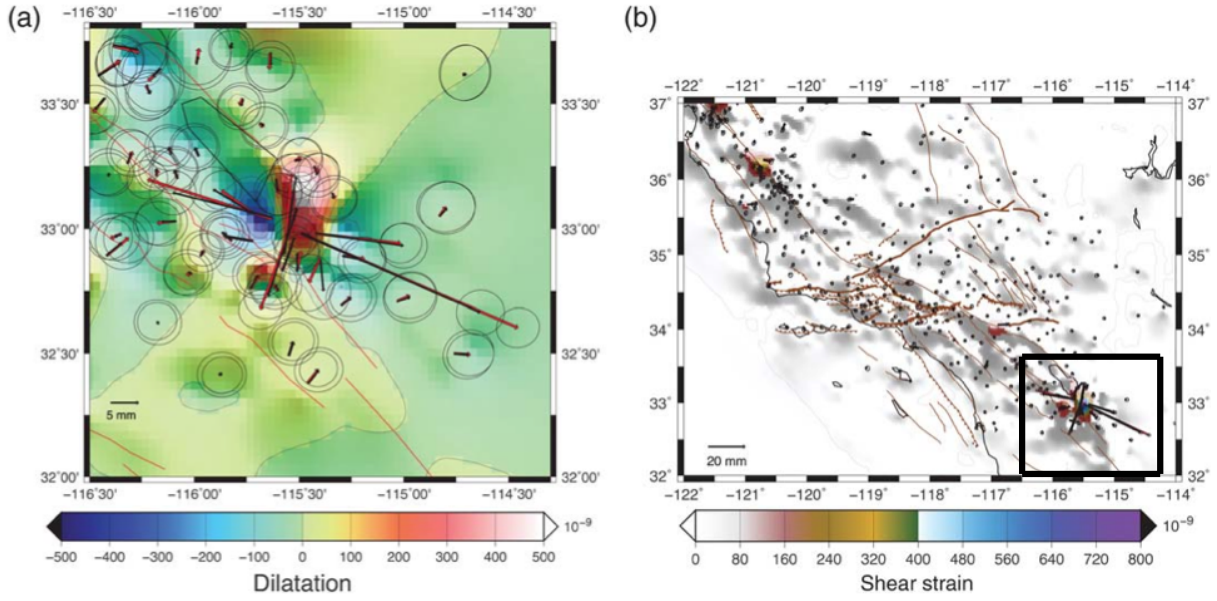

Figure 8. (**a**) Red vectors, observed displacement differences; bold vectors, model displacement differences (one-sigma standard error) on top of model dilatational strains from one-day solution on 26 August 2012. Large displacements and strains are associated with the Brawley swarm. The coseismic displacements are included in this solution. (**b**) Same as (a) but for the anomalous strains and displacements over the three month period between 8 August and 5 November 2012 on top of contoured shear-strain magnitudes, for all of southern California. Inset is region of (a).

2.6 - Discussion and Conclusions

One benefit of quantifying the full horizontal displacement gradient tensor field is that rotations and strains can yield insight into the dynamics of crustal deformation. For example, the anomalous strain tensor field can be used to infer stress tensor changes as a function of time. An incompressible elastic material [*Smith and Sandwell*, 2006; *Lutrell et al*., 2011] can be assumed to convert the strain tensor changes to model stress tensor changes. These stress tensor changes, together with a stress rate model obtained from the steady-state solution, can be used to better understand what regions during the transient process have been loaded closer to expected failure, as well as what regions have been pushed away from expected failure. The sign of the stress tensor change can be mapped with seismicity, using the location and moment tensor catalog from the Southern California Earthquake Data Center [*Hauksson et al*., 2012; *Yang et al*., 2012]. The spatial correlation of stress changes with seismicity occurrence can then be investigated. Because the postseismic signal decays non-linearly, most of the strain changes shown in Figure 11 occurred in the first year following the El-Mayor event. A more detailed retrospective analysis will, therefore, delineate the temporal evolution of the anomalous strain tensor field. Another feature that our solutions can offer is a better detail on the heterogeneous nature of some postseismic relaxation phenomenon. Such information may provide new constraints for rheological investigations [e.g., *Freed et al.*, 2007; *Pollitz et al*., 2012], including the possibility of resolving the effects of intrinsic heterogeneity and anisotropic properties of crust and upper mantle. The method we use is not confined to detection of shear dislocations on the faults, but can also be used to detect other sources, such as hydrologic [*Bawden*, 2003; *King et al*., 2007] and even non-tidal ocean loading [*Geng et al.*, 2012].

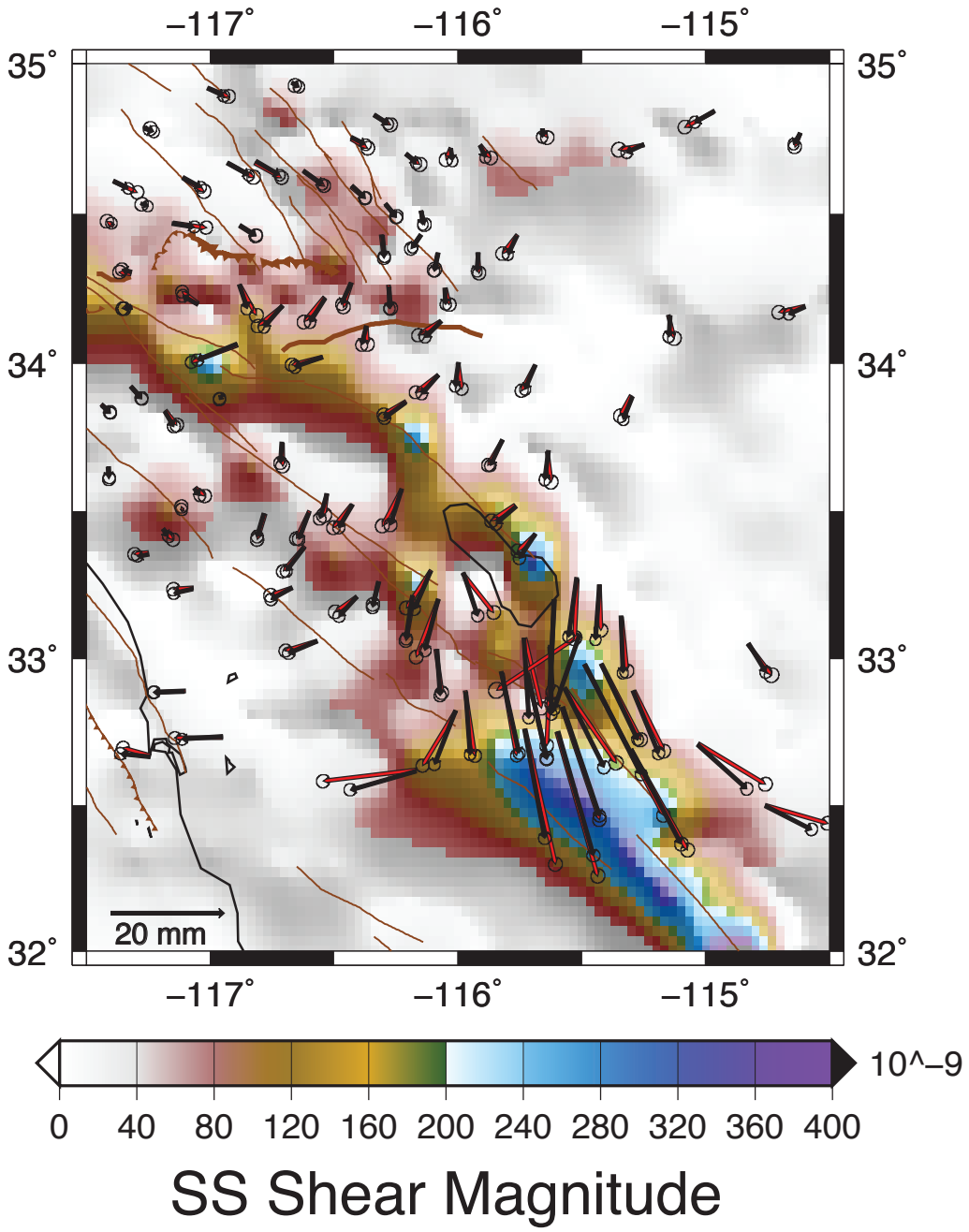

Figure 9. Anomalous strains and displacements during the period spanning (27 August 2010 – 27 August 2012). Red vectors, observed displacement differences; bold vectors, model displacement differences (95% confidence ellipse) on top of contoured model shear-strain-rate magnitudes (pure strike-slip style). The anomalous strain is dominated by the postseismic effects of El Mayor-Cucapah (see Fig. 10c for the distribution of the t-statistic that indicates where these anomalous strains are significant).

We have developed a cGPS network-processing tool for detection of anomalous strain over any desired time window. The key concept involved here is to determine a viable estimate of the horizontal displacement gradient field from the cGPS observations. Estimates of position, with estimates of seasonal signals removed, are interpolated to provide a model solution for the horizontal displacement gradient tensor field. The goal is to determine the sharpest image of the crustal strains and rotations permitted by the cGPS data. Benchmarking of the method, using output from a simple dislocation model [*Okada*, 1992], indicates that the GPS coverage is sufficient to provide a reliable geodetic reference solution, which is used to help determine if strains inferred from the cGPS observations are significant.

Regularization of the solution, obtained from the cGPS data, is achieved through (1) use of some *a priori* constraints on expected strain style (based on fault orientations); (2) use of an isotropic component of strain rate variance, which permits a departure of the model displacement field away from the expected orientation and magnitude of crustal strain. Adjusting the isotropic component of variance until the reduced chi-squared misfit between observed and model displacements approaches 1.0 yields optimal smoothing of the solution. The geodetic reference solution is subtracted from the epoch solution to determine anomalous patterns. The significance of these strains is tested using a t-statistic. Tests using synthetic cGPS observations, generated in the SCEC IV Transient Detection Exercise, show that anomalous strains associated with slow-slip over 6-8 week time frames, totaling less than 1 cm, can be detected with high confidence (assuming uncertainties in daily positions estimates of ± 3 mm). Analysis of PBO cGPS time series since July 2010 shows a complex field of significant anomalous strain primarily associated with postseismic processes.

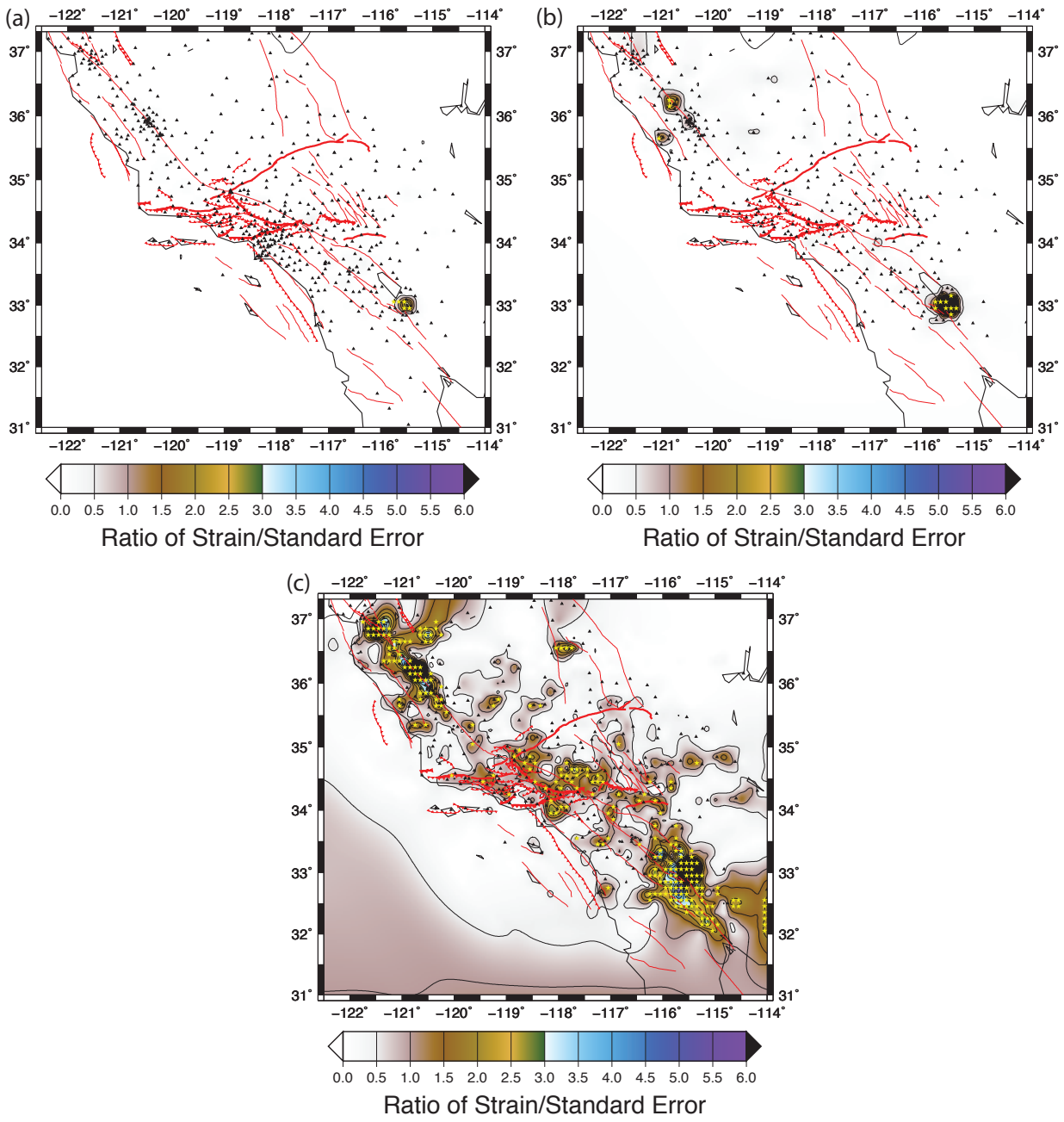

Figure 10. (**a**) Contour plot of t-statistic (equation 3) for one-day solution of 26 August 2012. Black triangles, location of cGPS stations; yellow stars, significant strains at 95% confidence or greater (t-statistic of 1.96 or greater). Bulls-eye in area of Brawley swarm, strains there are significant at much greater than 99% confidence. (**b**) Same as (a) but for accumulated strain between 10 August and 10 November 2012. **(c):** Same as (a) but for two-year period of strain accumulation (5 November 2010 – 5 November 2012).

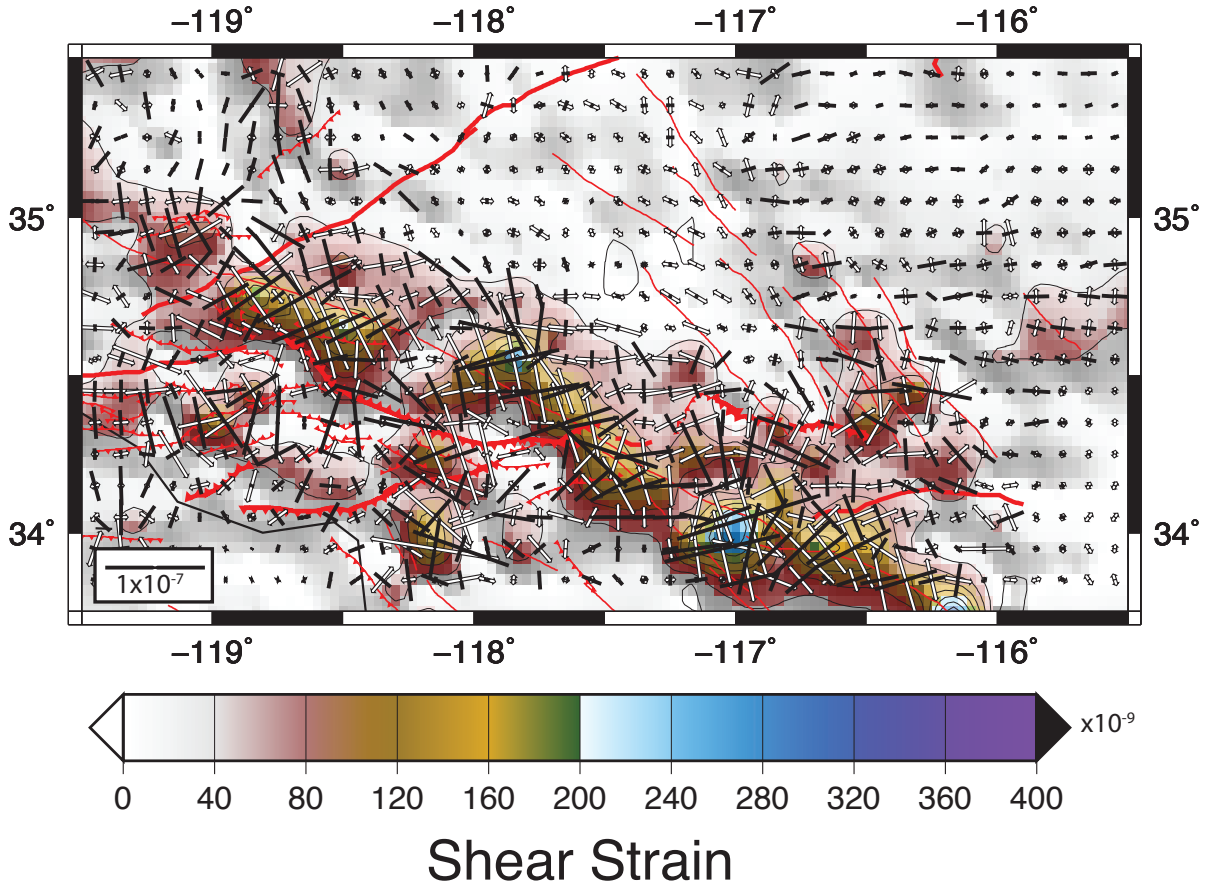

Figure 11. Plot of some of the anomalous strain accumulation (principal axes on top of contoured shear-strain magnitudes) over past 2 years within Southern California. Bold arrows, compressional strain; open arrows, extensional strain. The postseismic effects of El Mayor-Cucapah have caused many regions along the San Andreas and Eastern California Shear Zone to experience a sense of shear, which is opposite to the long-term loading (east-northeast-west-southwest-oriented principal axes of compressional strain and north-northwest-south-southeast principal axes of extensional strain). Other regions have experienced an increase in the direction of tectonic loading.

Chapter 3: El Mayor-Cucapah Postseismic Strain Evolution

3.1 - Introduction

The T-statistic test showed large areas of statistically significant anomalous strain in the Parkfield region, the Los Angeles Basin, and south of the Salton Sea (Figure 10c). The anomalous strain accumulation south of the Salton Sea is due to postseismic deformation created by the 2010 M7.2 El Mayor-Cucapah earthquake. The deformation is constrained to the San Andreas Fault System, and bounded by the strong Pacific lithosphere to the west and Central Valley lithosphere to the east [*Pollitz et al.,* 2012] and is consistent with the location and initial duration of the El Mayor aftershock sequence, which extended north to the US-Mexico border [*Hauksson et al.,* 2010]. This chapter describes an adaptation of the strain transient detection tool (Chapter 2) used to analyze this postseismic deformation.

3.2 - Adapting the Strain Transient Model to Analyze Postseismic Strain Evolution

In order to analyze the postseismic strains from the El Mayor (April 4, 2010) event leading up to the Brawley swarm (August 26, 2012), I produced a time-dependent horizontal displacement field using the method described in Chapter 2, with the one exception that the annual and semiannual signals were not removed from the time series. As was done previously, moving average filters were applied to the PBO time series (but without removing annual and semi-annual signals), and these averages were used to estimate displacements. Annual and semi-annual terms (calculated from coefficients *f,g,h* and *i* from Equation 2 in Chapter 3.2) were not deemed appropriate for the time series analysis here; immediate postseismic El Mayor deformation created a short-term curvature in the time series (Figure 12) and the estimation and

removal of annual and semi-annual terms had the potential to obscure this important postseismic signal. This does not diminish the value in estimating and removing the annual and semi-annual signals for strain transient detection; El Mayor postseismic strains, as well as anomalous strains in Parkfield and the Los Angeles Basin were detected using them in a longer-term retrospective analysis. Removal of annual and semi-annual terms is unnecessary for this specific analysis, which looks deeper into anomalous strain evolution over relatively short time epochs (0.1 and 0.12 years) associated with a known cause (the El Mayor event).

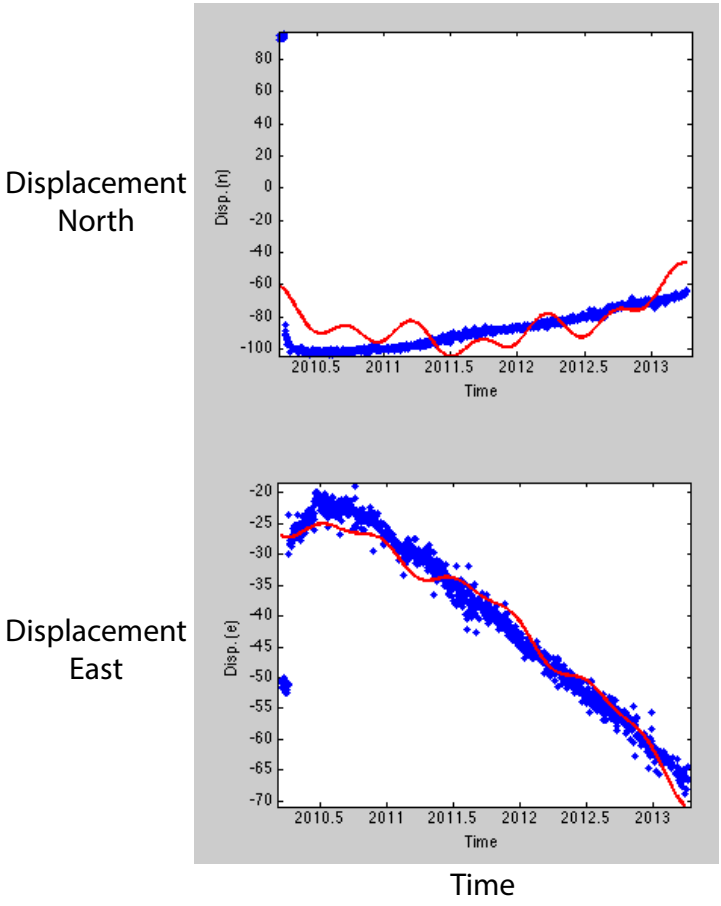

Figure 12. Time series (blue) for station P496 (244.40°W, 32.75°N) with annual and semiannual polynomial term (red line). Subtracting this calculated signal from the time series, as performed in Chapter 2, would have resulted in an incorrect solution for displacements and strain rates.

My initial qualitative examination of the time series for cGPS stations surrounding the event revealed that the time series for the first two postseismic epochs (first 0.24 years) varied so differently from the rest of the time series that they, along with the coseismic displacement, had to be analyzed separately (Figure 13). I separated each time series into 24 epochs; a one-day coseismic epoch at 2010.26 (day of event, 4 April 2010); 2 initial 0.12-year postseismic epochs, 2010.26 - 2010.38 ("ps1", 5 April – 18 May 2010) and 2010.38 – 2010.50 ("ps2", 19 May – 2 July 2010); and 21 final 0.1-year epochs, spanning 2010.50 – 2012.60 (3 July 2010 – 7 August 2012). I obtained the displacement estimate for the coseismic the way the daily analysis was performed in Chapter 2. I obtained the displacement estimate of ps1 by subtracting the first data point in this epoch (at 2010.26) from a moving average filtered point at 2010.38. All subsequent displacements, the second postseismic epoch, "ps2", and each 0.1-year epoch from 2010.50 – 2012.60, were estimated by subtracting the first moving average filtered point from the final moving average filtered point in each epoch, like the monthly estimates obtained in Chapter 2. Moving average windows 2 weeks in duration were deemed appropriate for capturing transients within 0.10 and 0.12 year intervals. A 2-week moving average window was long enough to smooth the data and reduce enough noise, yet short enough to capture transients within 0.1 and 0.12 year intervals.

In addition to obtaining the changes in displacement estimates for each epoch, I obtained cumulative displacements spanning multiple epochs by subtracting centered moving average estimates from the beginning and end of longer time epochs and adding them to the displacements estimates of ps1 and ps2. For example, the estimated displacement from 2010.50 - 2011.30, added to the displacements of ps1 and ps2, yields the cumulative estimated

displacement for the epoch 2010.26 through 2011.30. Cumulative displacement and strain estimates were calculated both including and excluding the coseismic displacement.

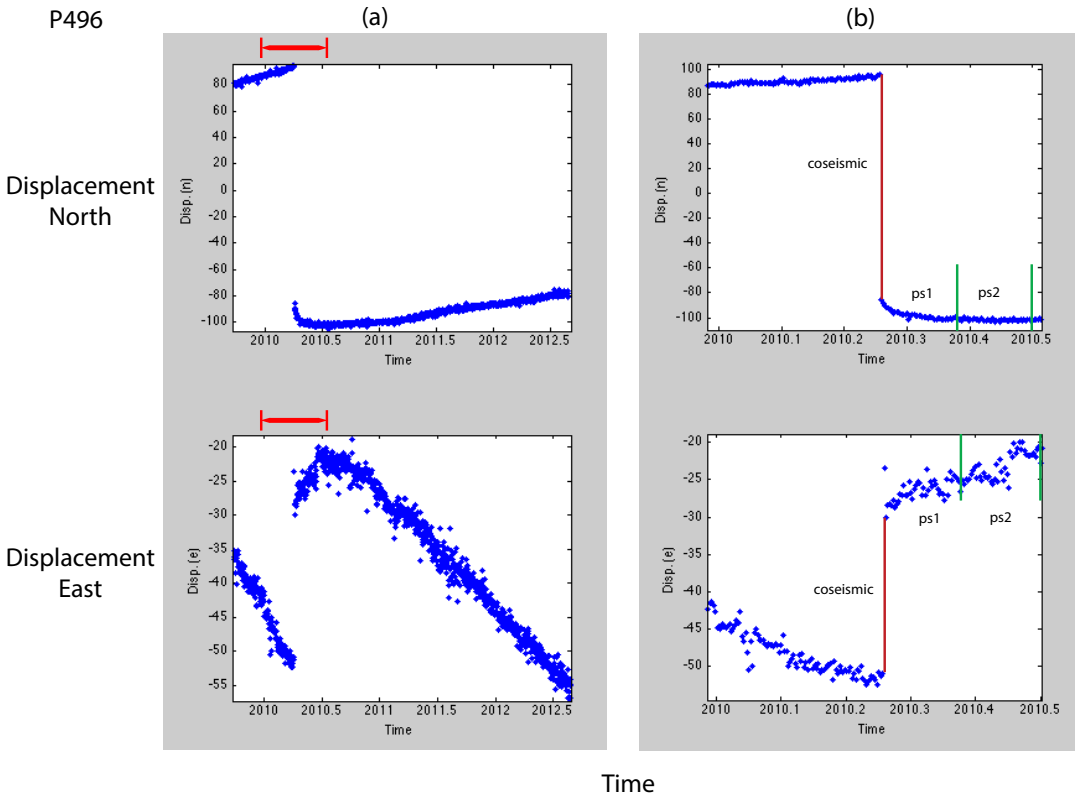

Figure 13. (**a**) Time series of station P496 (244.40°W, 32.75°N) showing complete time analyzed (including 4 April 2010 – 7 August 2012). Blue dots are raw cGPS data provided by the PBO observatory. Top, north-south displacement components; bottom, east-west displacement components. (**b**) Zoom-in of P496 time series, covering the timespan indicated by the red arrow-bar in (a) at left. Red line, coseismic displacement of the El Mayor event; green lines, bounds of qualitatively determined initial postseismic periods, "ps1" and "ps2".

3.3 – Anomalous and Total Deformation and Strain Results

In order to understand the complete evolution of El Mayor event postseismic strains, I first modeled total displacements and strains, and anomalous displacements and strains using the anisotropic constraint (Figures 14, 15, 16, & 17). The total displacement and strain (Figure 14a) represents the total strain accumulation over time, whereas the anomalous displacement and

strain (Figure 14b) shows the residual (anomalous) strain and displacement after the reference strain field is subtracted out. Finally, strains and displacements were modeled with an isotropic reference solution (Figure 22 a-d).

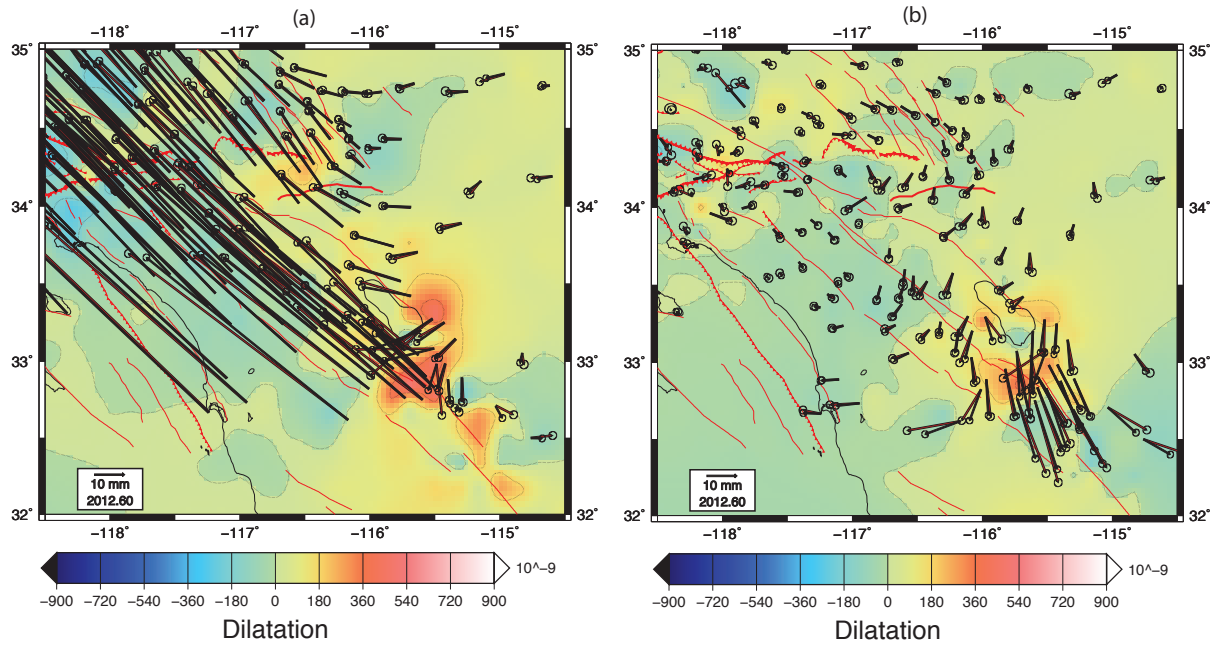

Figure 14. (**a**) Total and (**b**) anomalous displacements plotted on top of dilatational-strain magnitudes from 3 July 2010 – 7 August 2012. Red vectors, observed displacements; black vectors, modeled displacements.

Following the El Mayor event, the San Jacinto fault experienced no anomalous strain accumulation (Figure 15, 16), even though the displacement field (Figure 15) shows a broad long-wavelength anomalous clockwise rotation that develops over time. That is, the San Jacinto experienced a normal rate of strain accumulation (no shear strain anomaly along the San Jacinto in Figures 15a-d, 16a-d). The southern Elsinore fault zone, which connects in shear with the Laguna Salada fault where the El Mayor event ruptured, shows increased right lateral anomalous strains (compression north-south and extension east-west) with time (Figure 16a-d). These strains grow more rapidly relative to other area strains, but at a steady rate.

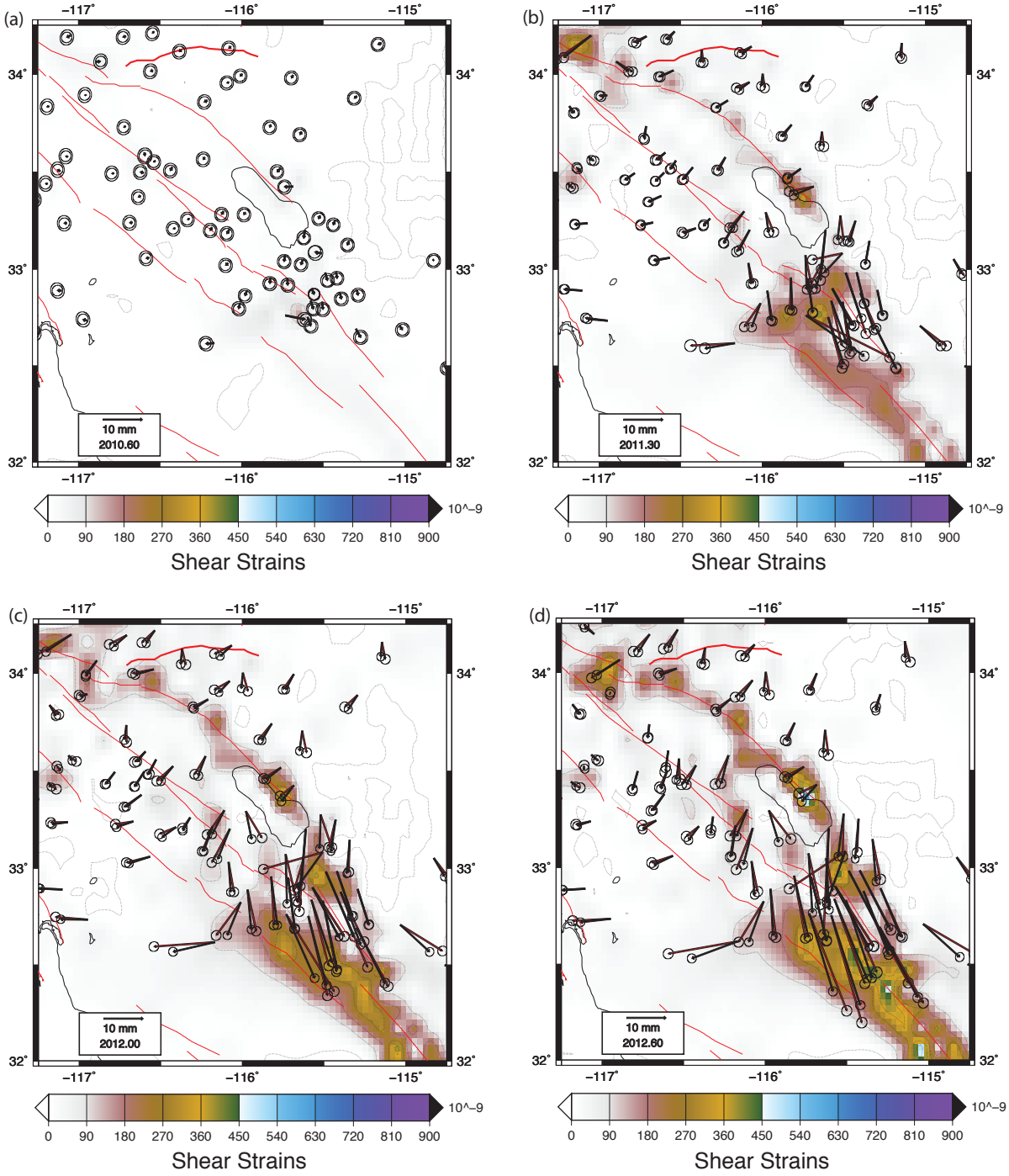

Figure 15. Anomalous displacements (red, model; black, observed) plotted over contoured anomalous shear strain magnitudes spanning 4 epochs; (**a**) 3 July 2010 – 7 August 2010, (**b**) 3 July 2010 – 19 April 2011, (**c**) 3 July 2010 – 31 December 2011, (**d**) 3 July 2010 – 7 August 2012. Error ellipses are plotted at 95% confidence.

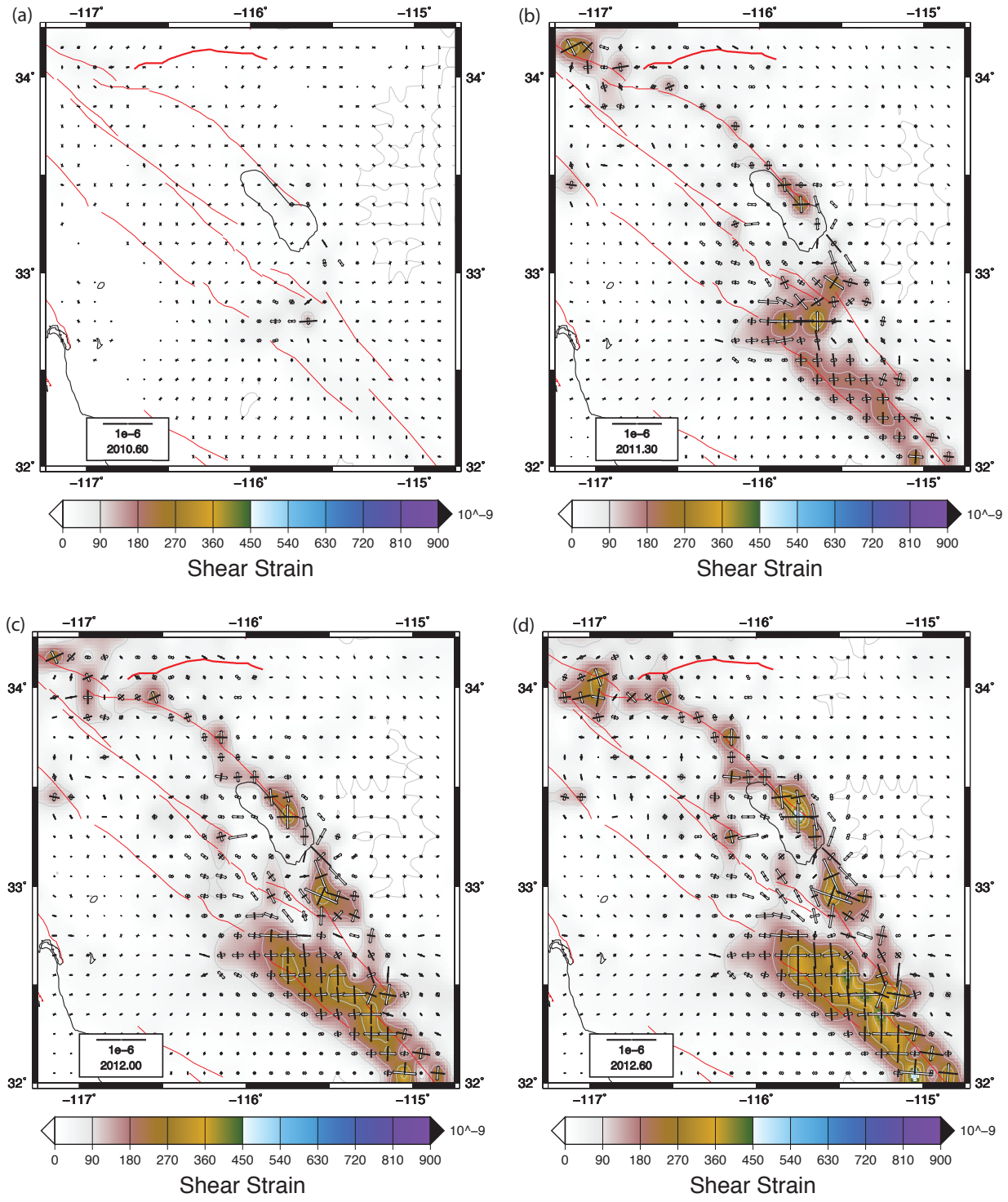

Figure 16. Principal axes of anomalous strain (bold arrows, compressional; open arrows, extensional) plotted over contoured anomalous shear strain magnitudes spanning 4 epochs; (**a**) 3 July 2010 – 7 August 2010, (**b**) 3 July 2010 – 19 April 2011, (**c**) 3 July 2010 – 31 December 2011, (**d**) 3 July 2010 – 7 August 2012.

The Southern San Andreas slowly develops shear strain up to 100 x 10^{-9} until 2011.1, at which point strain accumulation became even slower, and increased by 80 x 10^{-9} over the next 0.7 years (Figure 15a-c). At 2011.9, shear strain accumulation increased more rapidly, and maximizes at 300 x 10^{-9} in some areas at 2012.6 (Figure 15d). The principal axes of anomalous strain along the southern San Andreas Fault are oriented with extension E-W and compression N-S, which is a left-lateral sense of anomalous shear (Figure 16, 17). That is, total shear strain rates, defined by the GPS, along this section of the fault are pure right-lateral shear, but are accumulating at a lower rate than the reference solution (thus the left-lateral anomalous shear) (Figure 15d, 19).

The Brawley Seismic Zone is the area between the southern San Andreas and the Imperial Fault, south of the Salton Sea. Two larger extensional strains develop here, one to the north and one to the south of a pocket of compression (Figure 17a-d). The northern extensional area is consistent with the left-lateral anomalous strain along the southernmost San Andreas on the southeast end of the Salton Sea. The compressional pocket remains fairly small but increases gradually, going from 0 - 200 x 10^{-9} over 2 years until the Brawley swarm of August 26, 2012. A movie of the strain evolution shows an interesting strain evolution of the region including and surrounding the area that eventually ruptured in the 2012 Brawley swarm. Both extension and shear dominate here, where principal axes of strain are N-S to NW-SE (Figures 16, 17), which is consistent with the style of the Brawley swarm earthquakes (Figure 18) [Hauksson et al., 2013]. The development of anomalous NW-SE oriented extension in the Brawley zone region may have been responsible for unclamping the left-lateral structures that ruptured in the Brawley zone. In the vicinity of the area that ruptured in the Brawley swarm, extensional principal axes rotate counterclockwise by about 20° over the 2 year postseismic period.

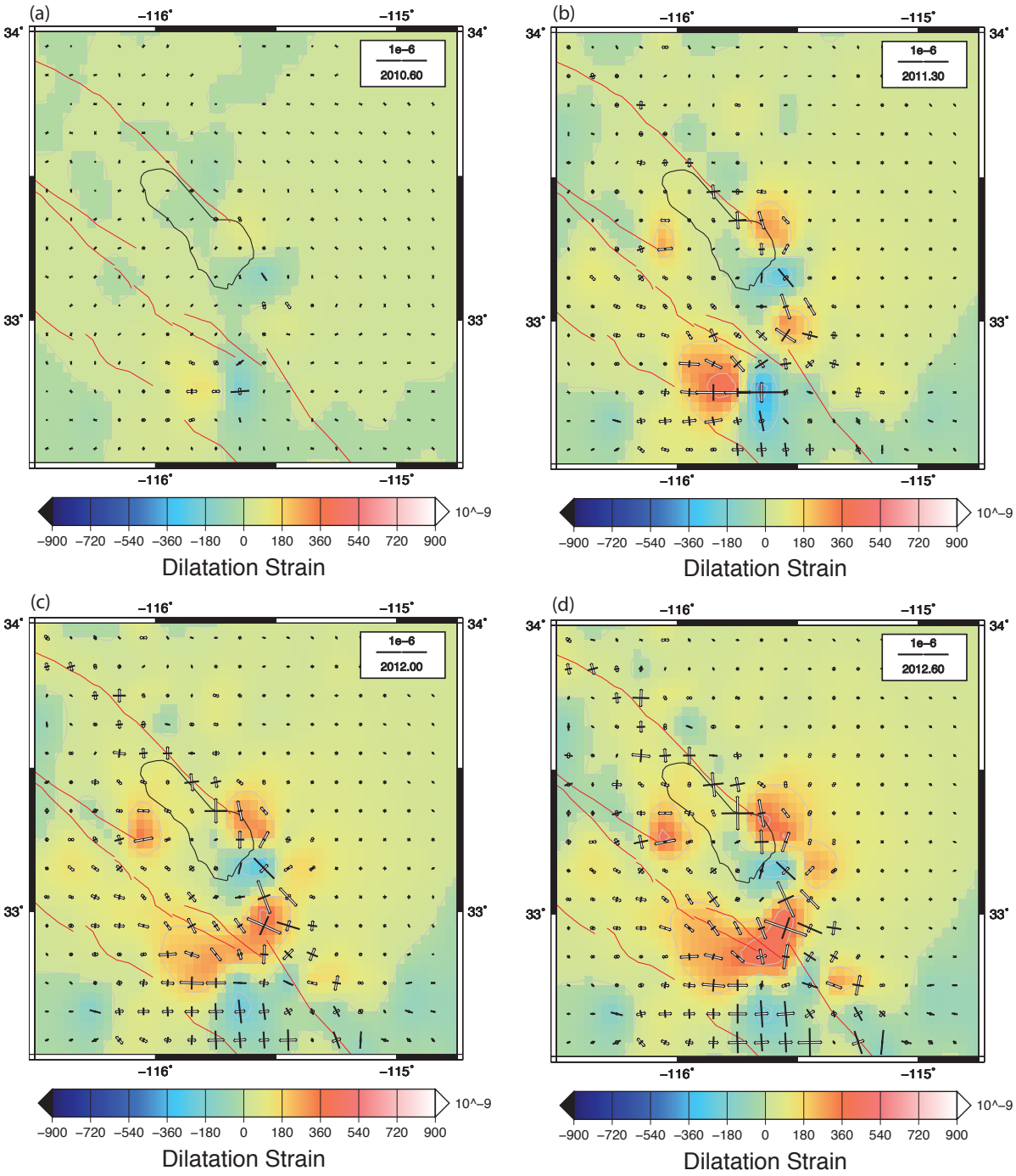

Figure 17. Principal axes of anomalous strain (bold arrows, compressional; open arrows, extensional) plotted over contoured anomalous dilatational strain magnitudes spanning 4 epochs; (**a**) 3 July 2010 – 7 August 2010, (**b**) 3 July 2010 – 19 April 2011, (**c**) 3 July 2010 – 31 December 2011, (**d**) 3 July 2010 – 7 August 2012. Brawley Seismic Zone dilatational strain anomalies at approximately 33°N, -115.5°W.

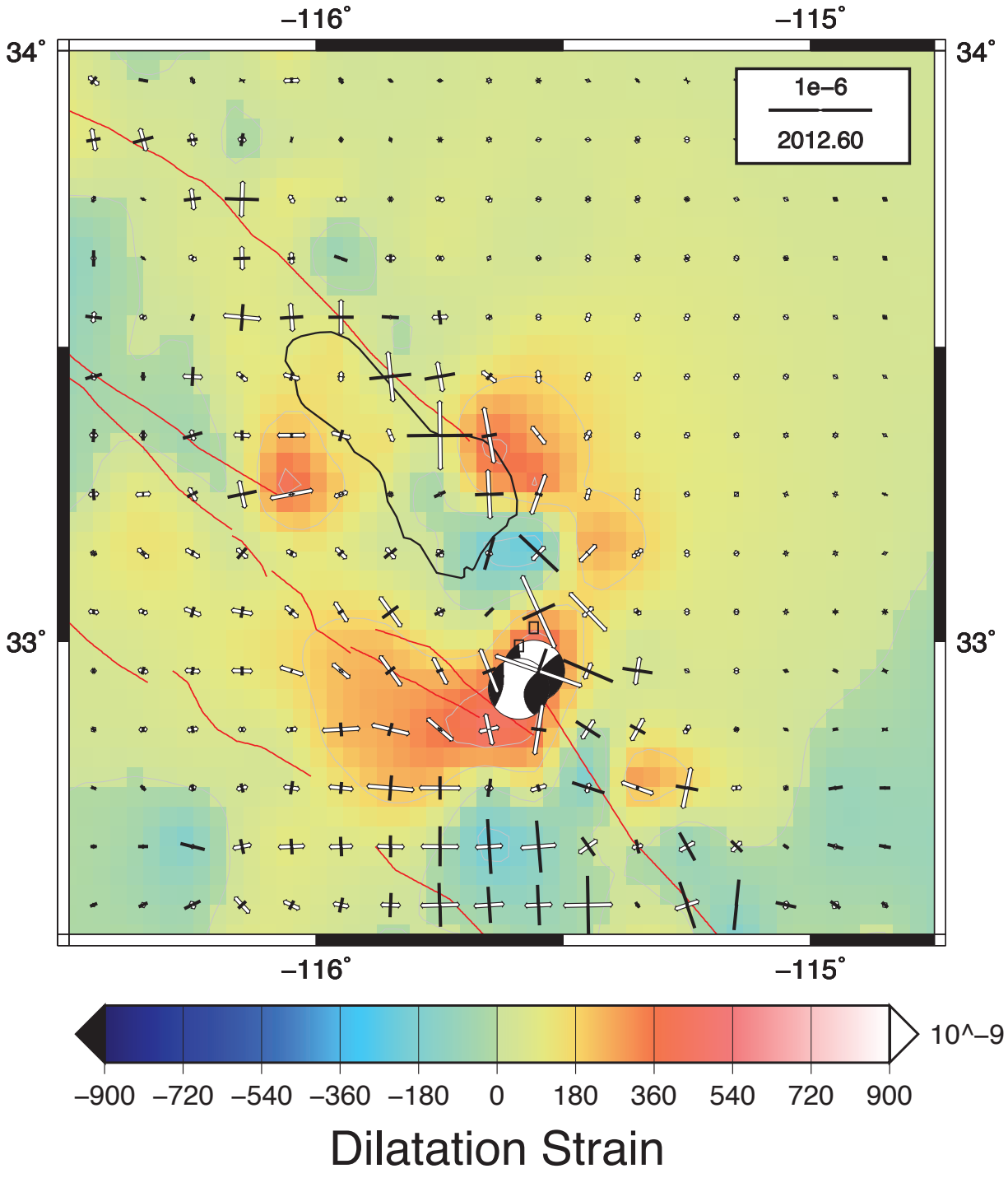

Figure 18. Focal mechanisms for the 2 largest (M5.4) events of 26 August 2012 Brawley Swarm (*Dziewonski et al.*, 1981; *Ekström et al.*, 2012**)** plotted with anomalous principal strain axes (bold arrows, compressional; open arrows, extensional) and anomalous dilatational strain contours spanning 7 July 2010 – 8 August 2012.

3.3.1 – Isotropic Analysis

The previous analysis utilizes some *a priori* information about the orientation and style of faulting within the region of study. It is important to understand how this *a priori* information influences the anomalies described in the previous section, and how the model would behave without this information. In the anisotropic analysis described above, the structure of the variance-covariance matrix V_{ijkl} in (1) incorporates information about fault location, strike, and expected style of slip [*Shen-Tu et al.,* 1999]. The variances and covariances are obtained with

$$\mathrm{Var}\left(\bar{\dot{\varepsilon}}_{ij}\right) = \sum_{k=1}^{n}\left(\frac{L_k \dot{u}_k^d}{2A\ sin\delta_k} m_{ij}^k\right)^2 + (\varepsilon)^2\left[\frac{1}{2}\left(1 + \delta_{ij}\right)\right] \tag{4}$$

and

$$\mathrm{Cov}\left(\bar{\dot{\varepsilon}}_{ij}, \bar{\dot{\varepsilon}}_{pq}\right) = \sum_{k=1}^{n}\left(\frac{L_k \dot{u}_k^d}{2A\ sin\delta_k}\right)^2 \left(m_{ij}^k m_{pq}^k\right) \tag{5}$$

from *Shen-Tu et al.* (1999), where L_k is the length of the fault that crosses a given area, A (0.1°x0.1° grid), δ_k is the fault dip, $\dot{u}_k^d$ is the uncertainty in fault slip rate, ε is the isotropic component of uncertainty, m_{ij}^k is the unit moment tensor of the fault, and δ_{ij} is the Kronecker delta. This data is taken from known quaternary fault information [*Jennings,* 1994], and provided by *Shen-Tu et al.* (1999).

Equation (4) is composed of 2 parts. The first term in (4) is anisotropic and inhomogeneous and contains known quaternary fault information (Figure 19, 20). The unit moment tensor provides the relative values of xx, yy, and xy, which yields information on expected orientation and relative magnitudes of the principal axes of strain. If the model strains follow the *a priori* expected orientations, then these strains would be consistent with the style of faulting (strike-slip, dip-slip, or mixed) present in the Quaternary fault data base that we used [*Jennings*, 1994; *Shen-Tu et al*., 1999] . The covariances influence how the cGPS observations are interpolated (Figure 20). For example, the objective function (1) is penalized by putting in model strains that differ significantly from the expected direction of principal axes and relative magnitude of principal axes (based on fault data). This *a priori* information on direction and relative magnitude of principal axes is not a strict constraint. That is, it may be required that the model strains differ significantly from expected in order to fit the cGPS observations. In addition, the inhomogeneous distribution of strain rate variances (Figure 19) means that the objective function is penalized less for putting in large strains within these regions of higher strain rate variance. The second part of the variance-covariance matrix (the isotropic portion in (4)) is adjusted until the cGPS are adequately matched within the region of interest.

In order to test how this *a priori* information affects the realization of strain anomalies, a separate analysis was performed using an isotropic and homogeneous variance-covariance matrix. Here, the anisotropic portion of (4) (i.e., the first term in (4)) is not included, lending no fault information to the model. The isotropic portion of (4) (i.e., the second term of (4)) was adjusted for each epoch to obtain a reduced chi-squared misfit between model and observed cGPS close to 1. Furthermore, the covariances for all areas are 0; there is no expected direction

or relative magnitude for the principal axes of strain. The construction of V_{ijkl} here is thus isotropic and homogeneous (Figure 21).

Isotropic variances of strain give the cGPS data primary control on the realization of the model strain field. That is, there are no built-in *a priori* constraints about the expected style and orientation of the strain field. The comparison of the isotropic and anisotropic solutions enables us to test how much of the strain model is controlled by the cGPS data versus the role and importance of additional constraints on the expected style of strain and, to a much lesser extent, expected magnitude of strain.

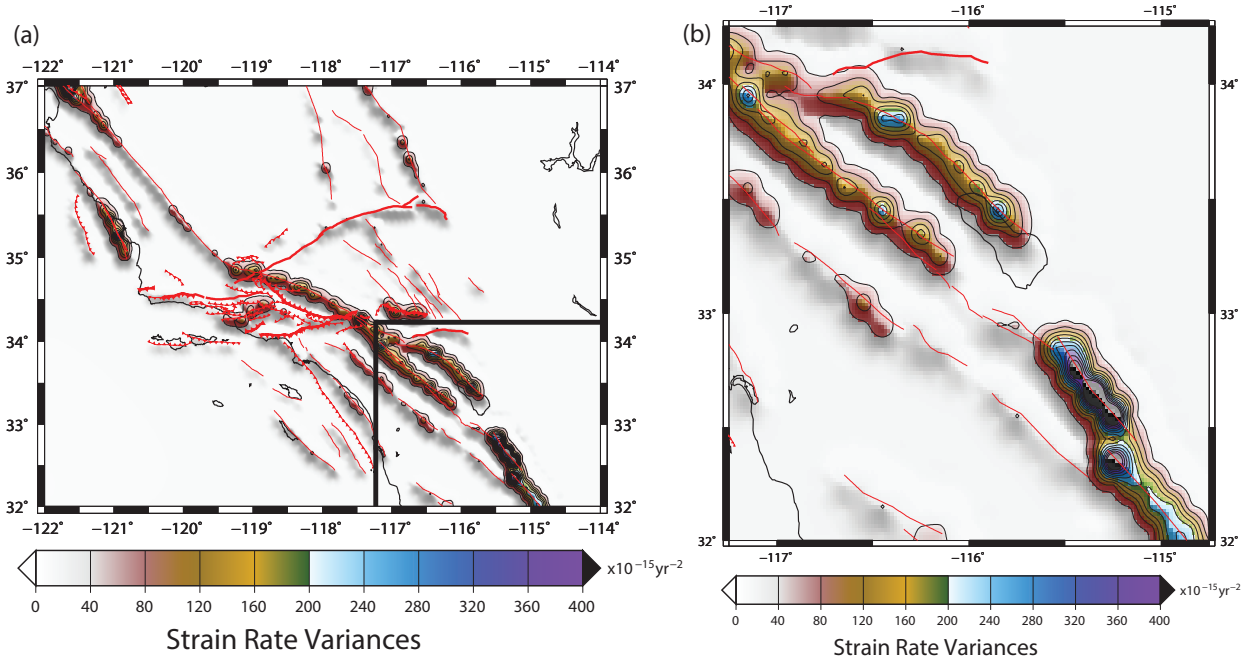

Figure 19. Magnitude of the variances, defined by Var(xx) + Var(yy) + 2*Var(xy), for the anisotropic solution of the (**a**) entire region. (**b**) Inset of (a).

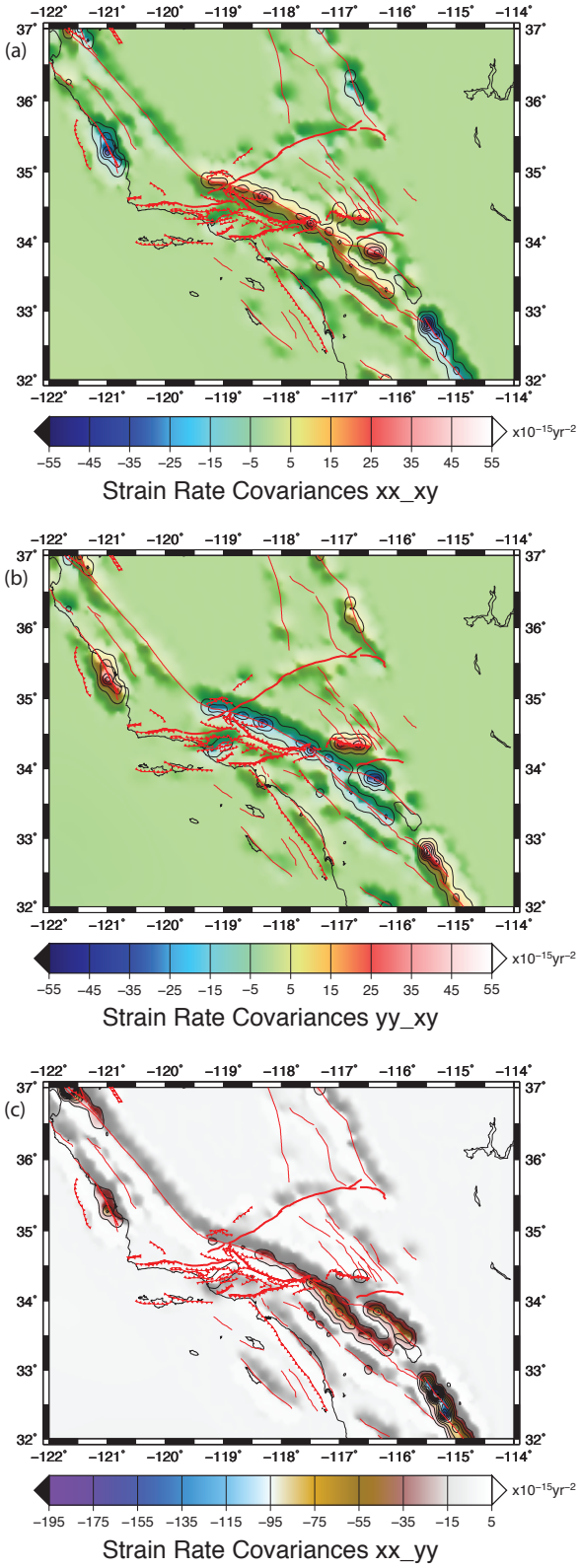

Figure 20. For the anisotropic solution, (**a**) covariances between xx and xy, (**b**) covariances between yy and xy, and (**c**) covariances between xx and yy.

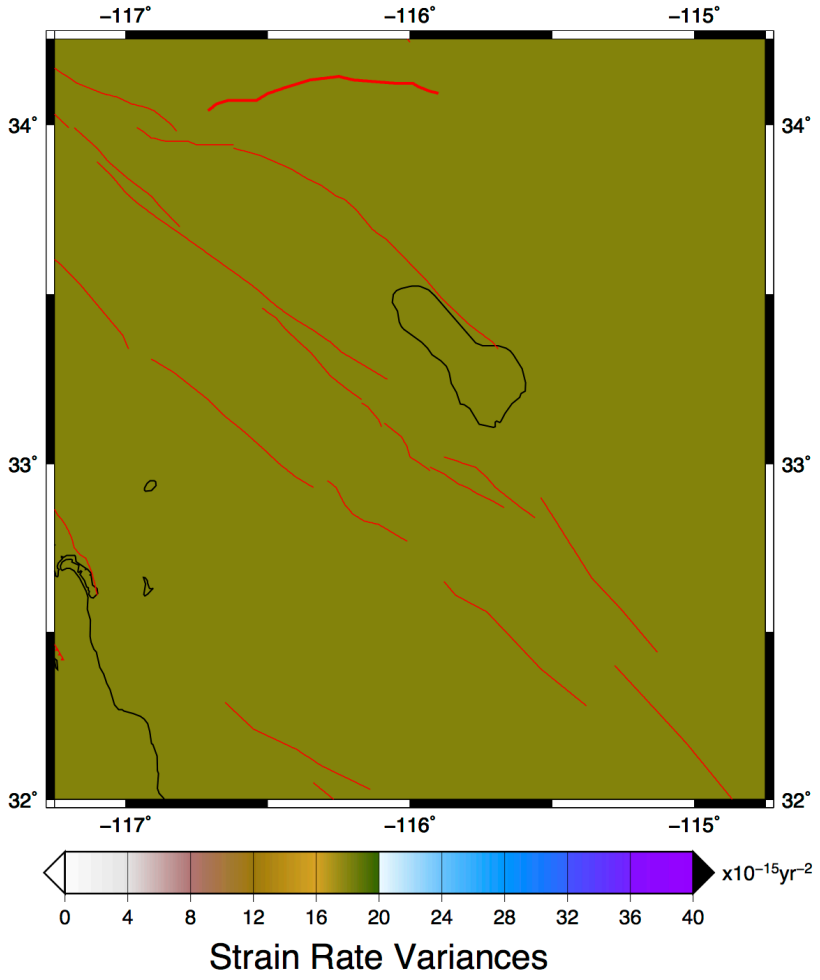

Figure 21. Magnitude of the variances, defined by Var(xx) + Var(yy) + 2*Var(xy), for the isotropic solution. The value is constant everywhere at 18.

Anomalous shear strains along the southern segment of the Elsinore fault zone from the isotropic homogeneous solution are right-lateral, like the anisotropic, but their final magnitudes are about 150 x 10^{-9} yr^{-1} lower (Figure 15, 18, 22). The results from the isotropic solution are nearly identical to the anisotropic along the San Jacinto fault (Figure 15, 18, 22). Anomalous shear strains along the southernmost San Andreas Fault are left-lateral, like the anisotropic, but their magnitudes are 100 x 10^{-9} yr^{-1} lower than the final strain accumulation along this section of the fault, and about 250 x 10^{-9} yr^{-1} lower where the southern San Andreas fault terminates, just

north of the Brawley Seismic Zone (Figure 22). In the Brawley Seismic Zone, the isotropic homogeneous solution produces anomalous shear strains oriented the same way as the anisotropic solution, but with a shear anomaly about 50 x 10^{-9} yr^{-1} larger and 0.1° north of the largest shear anomaly in the anisotropic (Figure 22).

The southernmost anomalous dilatational strain in the Brawley Seismic Zone is the same for both the isotropic and anisotropic solutions (Figure 23). However, the compressional pocket in the Brawley Seismic Zone, as well as the northernmost area of extension (at the termination of the San Andreas Fault), is about 75 x 10^{-9} yr^{-1} larger in the isotropic solution (Figure 24).

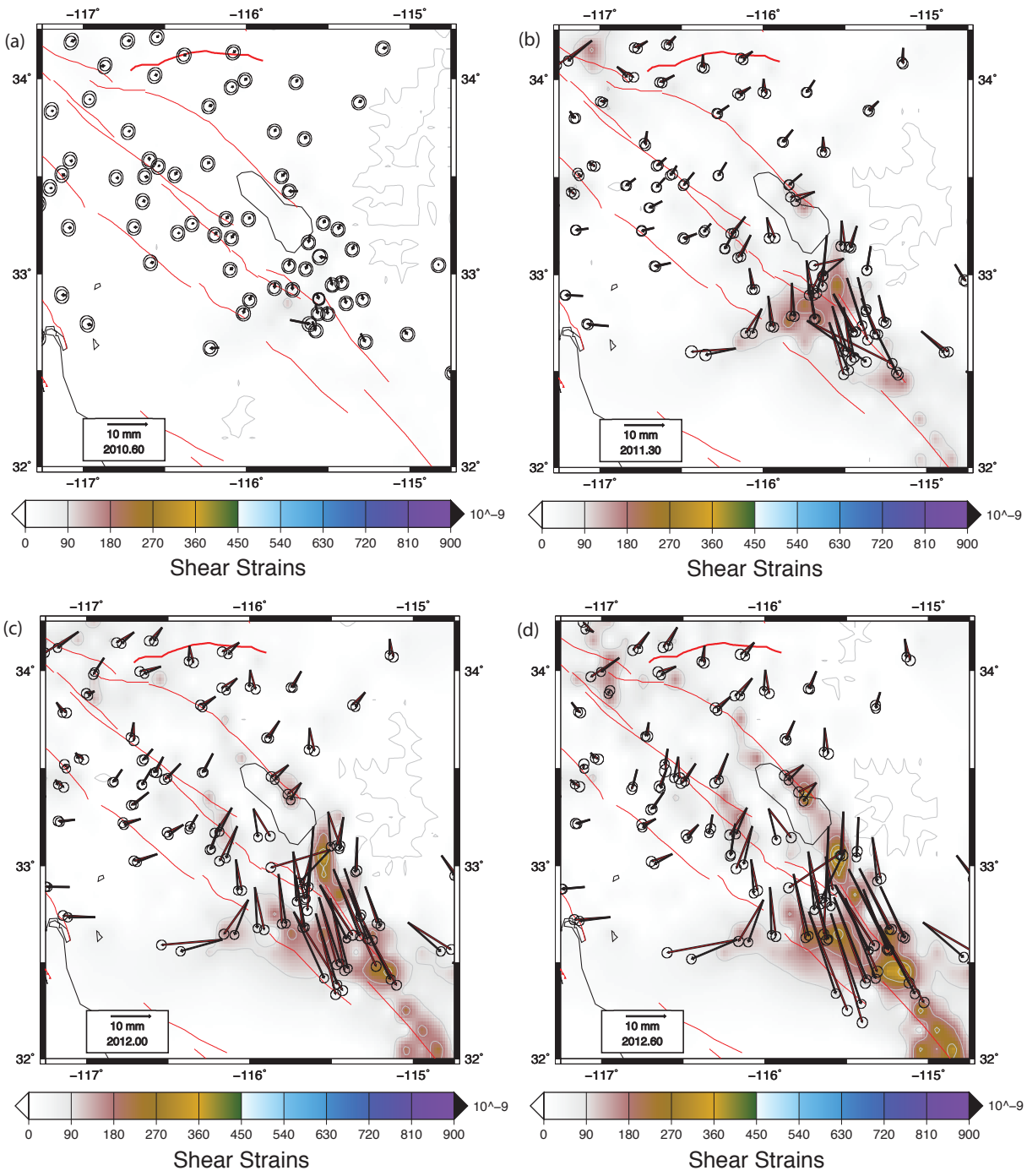

Figure 22. Anomalous displacements (red, model; black, observed) plotted over contoured anomalous shear strain magnitudes spanning 4 epochs; (**a**) 3 July 2010 – 7 August 2010, (**b**) 3 July 2010 – 19 April 2011, (**c**) 3 July 2010 – 31 December 2011, (**d**) 3 July 2010 – 7 August 2012. Error ellipses are plotted at 95% confidence. Fitting is based on isotropic homogeneous solution.

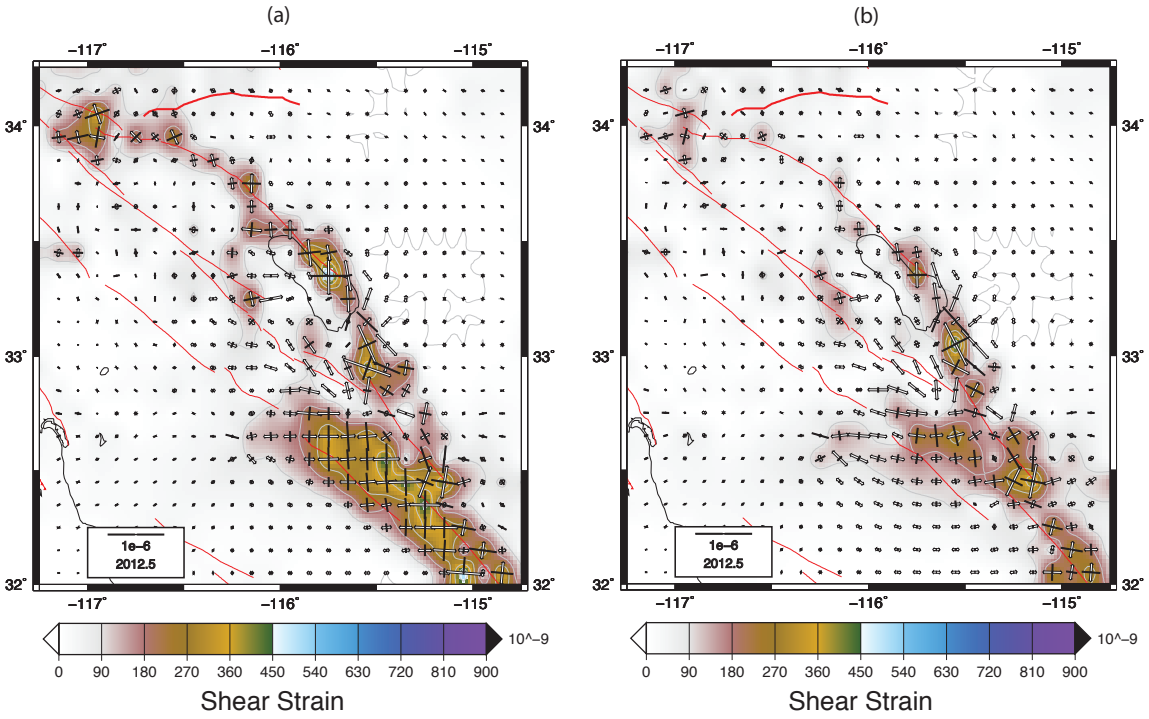

Figure 23. Principal axes of anomalous strain (bold arrows, compressional; open arrows, extensional) plotted over contoured shear strain magnitudes spanning 3 July 2010 – 7 August 2012. (**a**) Anisotropic, (**b**) isotropic.

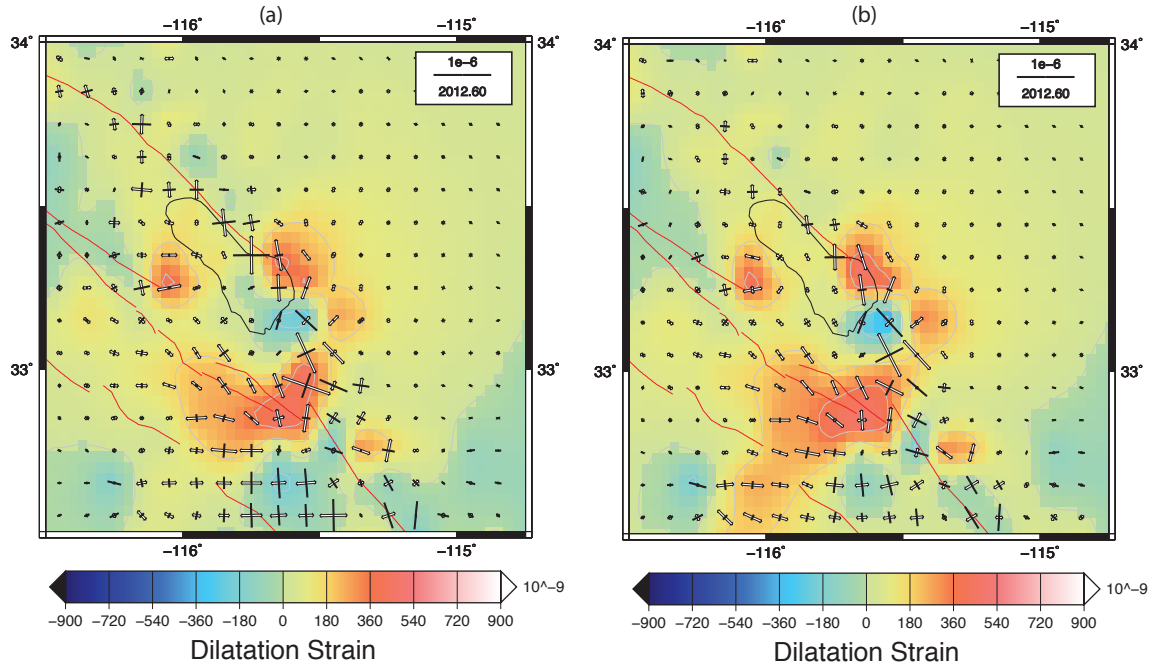

Figure 24. Principal axes of anomalous strain (bold arrows, compressional; open arrows, extensional) plotted over contoured dilatational strain magnitudes spanning 3 July 2010 – 7 August 2012. (**a**) Anisotropic, (**b**) isotropic.

3.4 – Discussion and Conclusion

A striking feature of both the anisotropic and isotropic anomalous strain models is the anomalous strain field in the Brawley Seismic Zone. The Brawley Seismic Zone is an interesting area of the San Andreas Fault Zone, as it experiences rotation and extension [*Crowell et al.,* 2013] which may eventually cause it to become a rifting area similar to the Gulf of California (*Smith and Sandwell,* 2003], it is subjected to aseismic creep [*Lohman and McGuire,* 2007, *Llenos and McGuire,* 2011] and it is one of the most seismically active regions in California [*Larsen and Reilinger,* 1991]. My anisotropic solution is consistent with the anomalous shear strain, extensional strain, and counterclockwise strain rotations south of the Salton Sea modeled by *Crowell et al.* 2013. The strain evolution presented here may also be used with seismicity rates to help improve our understanding of the aseismic processes of the Brawley Seismic Zone [*Lohman and McGuire,* 2007]. Overall, this tool which uses cGPS data to determine a strain evolution of the Brawley Seismic Zone has the potential to help us better understand this fascinating section of the San Andreas Fault Zone.

The anomalous anisotropic principal strain axis field along the Southern San Andreas Fault is another prominent feature of this postseismic strain evolution. When modeled from the long-term steady state solution, these axes are oriented with compression in the north-south direction and extension in the east-west direction (Figure 25). The anomalous strain principal axes along the southern San Andreas are in the opposite direction, which implies that this section of the fault is experiencing a reduced rate of shear (in comparison to the reference model) during the postseismic period. To verify that this is a direct result of the El Mayor event, the credibility of the cGPS data and the observed strains prior to the event would have to be assessed.

The isotropic solution preserves the shear anomaly along the Southern San Andreas, which indicates that this is a robust feature constrained by the cGPS, and it is not an artifact of our *a priori* constraints on fault style. Although no fault information was provided in the model, these cGPS-dependent strains were modeled in the same style and location as the anisotropic solution.

The strain anomaly along the southern San Andreas may indicate that the El Mayor event changed the rate of strain accumulation along the Southernmost San Andreas Fault. These anomalous strains should be reflected in a stress change solution. The fault experiences extension where it would usually experience compression, so a negative Coulomb stress change should be observed here. These strain evolution models can be used to calculate stress changes with time. An improved understanding of the stress evolution after the El Mayor event can be used to forecast seismicity in this region by incorporating these stress changes into the rate/state stress transfer model [*Toda et al.,* 2005].

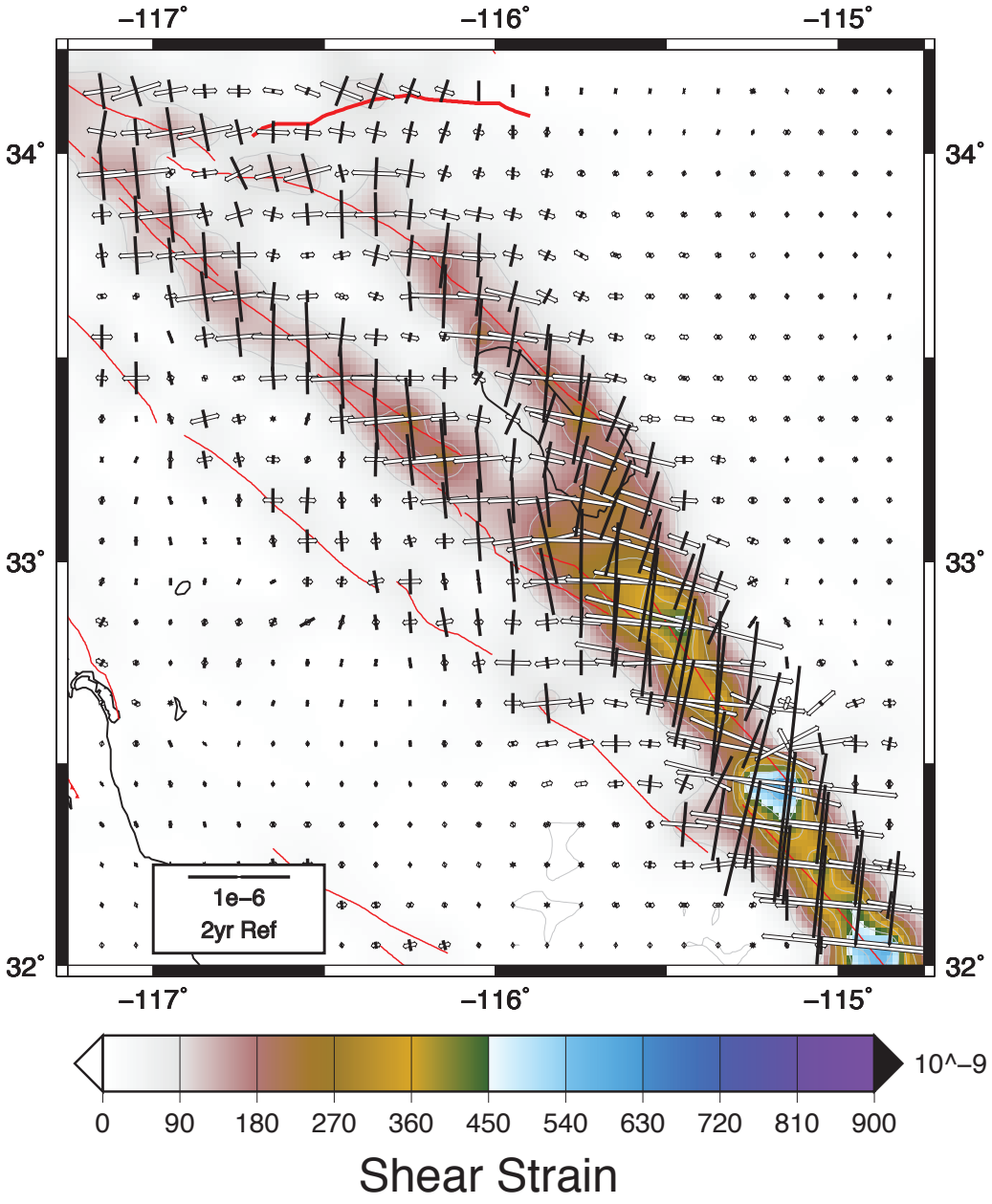

Figure 25. Principal axes of strain of the anisotropic reference solution scaled to 2 years, plotted over shear strain magnitude contouring. Bold arrows, compressional (primarily north-south); open arrows, extensional (primarily east-west).

Chapter 4 – Coulomb Stress Changes

4.1 - Introduction

Anomalous strains along the southern San Andreas Fault were estimated to show extension in the north-south direction and compression in the east-west direction. These indicate a reduced rate of strain accumulation on the Southernmost San Andreas Fault, and such changes should be reflected in Coulomb stress change estimates for that region. This section of the fault should experience a negative stress change (or total stress changes that are lower than the expected secular rate). Conversely, increased anomalous strain rates in the direction of long term loading along the southern Elsinore Fault and within the Brawley Seismic Zone should indicate positive Coulomb stress changes. The San Jacinto Fault should experience little to no anomalous stress changes within this postseismic period.

4.2 – Coulomb Stress Change Calculation

In order to properly calculate time-dependent Coulomb stress changes for this area, it is necessary to know the orientation of faults that are subjected to the changes in the stress field, obtained from our time-dependent strain solutions. The angle ψ is defined as the angle between the fault plane and the x-axis (Figure 26) [*King et al.,* 1994]. Stress changes act on this plane.

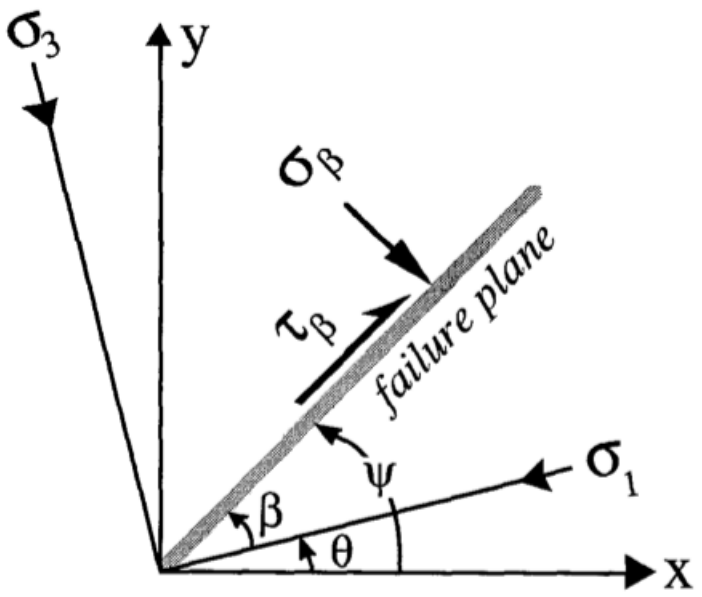

Figure 26. Schematic of variables associated with calculating the optimal failure plane angle ψ, from *King et al*., 1994.

One option is to use the Quaternary fault data base to obtain the orientations of the faults that are subjected to the stress changes. Another option is to use information embedded in the steady-state strain field solution (Figure 2, Chapter 2). For example, *Holt and Haines* (1993) showed that the expected fault orientation, ψ, can be obtained from any horizontal strain field; I apply this relation to the steady state strain rate tensor solution defined by the SCEC4.0 velocity field (Figure 2, Chapter 2) to obtain orientations of shear planes. Two solutions for ψ exist

$$\tan\psi = \left(\frac{-\dot{\varepsilon}_{xy} \pm \sqrt{\dot{\varepsilon}_{xy}^{\,2} - \dot{\varepsilon}_{xx}\,\dot{\varepsilon}_{yy}}}{\dot{\varepsilon}_{yy}}\right) \tag{6}$$

that correspond to the possible no-length-change directions, or the strikes of fault planes that would explain the horizontal strain field [*Holt and Haines*, 1993]. If the 2 solutions of ψ are equal, the fault is purely normal or reverse. When the 2 solutions for ψ are orthogonal, the fault

is vertical strike slip. The reference strain rate solution is consistent with nearly pure vertical strike slip faults along the southern San Andreas portion, as indicated by the orthogonal no-length-change orientations (Figure 27) [*Holt,* 2014].

I followed the methods of *King et al.* (1994), who provided the appropriate strain to stress change equations for vertical strike slip faults. Normal and shear stresses are calculated by

$$\sigma_{11} = \sigma_{xx}\cos^2\psi + 2\sigma_{xy}\sin\psi\cos\psi + \sigma_{yy}\sin^2\psi$$

$$\sigma_{33} = \sigma_{xx}\sin^2\psi - 2\sigma_{xy}\sin\psi\cos\psi + \sigma_{yy}\cos^2\psi$$

$$\tau_{13} = \tfrac{1}{2}\left(\sigma_{yy} - \sigma_{xx}\right)\sin 2\psi + \tau_{xy}\cos 2\psi \qquad (7)$$

where σ_{xx}, σ_{yy}, and σ_{xy} are the stress changes obtained from the time-dependent strain solutions. The change in Coulomb stress for a right lateral, vertical fault is thus

$$\sigma_f^R = \tau_{13}^R + \mu'\sigma_{33} \quad , \qquad (8)$$

where τ_{13}^R is the shear stress resolved on the fault and σ_{33} is the normal stress resolved on the fault.

In order to determine an effective coefficient of friction, μ', a μ' = 0.4 [*Toda et. al*, 2005] and μ' = 0.6 [*Smith and Sandwell*, 2003] were tested, and the stress changes were quite similar (Figure 28, 29). Since these results would be used in a future study of forecasting the evolution of seismicity, I decided to remain consistent with *Toda et al.* (2005), and I used a μ '= 0.4 to calculate stress changes on both right lateral and left lateral structures. In a vertical strike-slip

fault regime (containing horizontal x and y axes and displacements), the left lateral stress change is the same as for the right, but with the sign of τ reversed [*King et al.,* 1994].

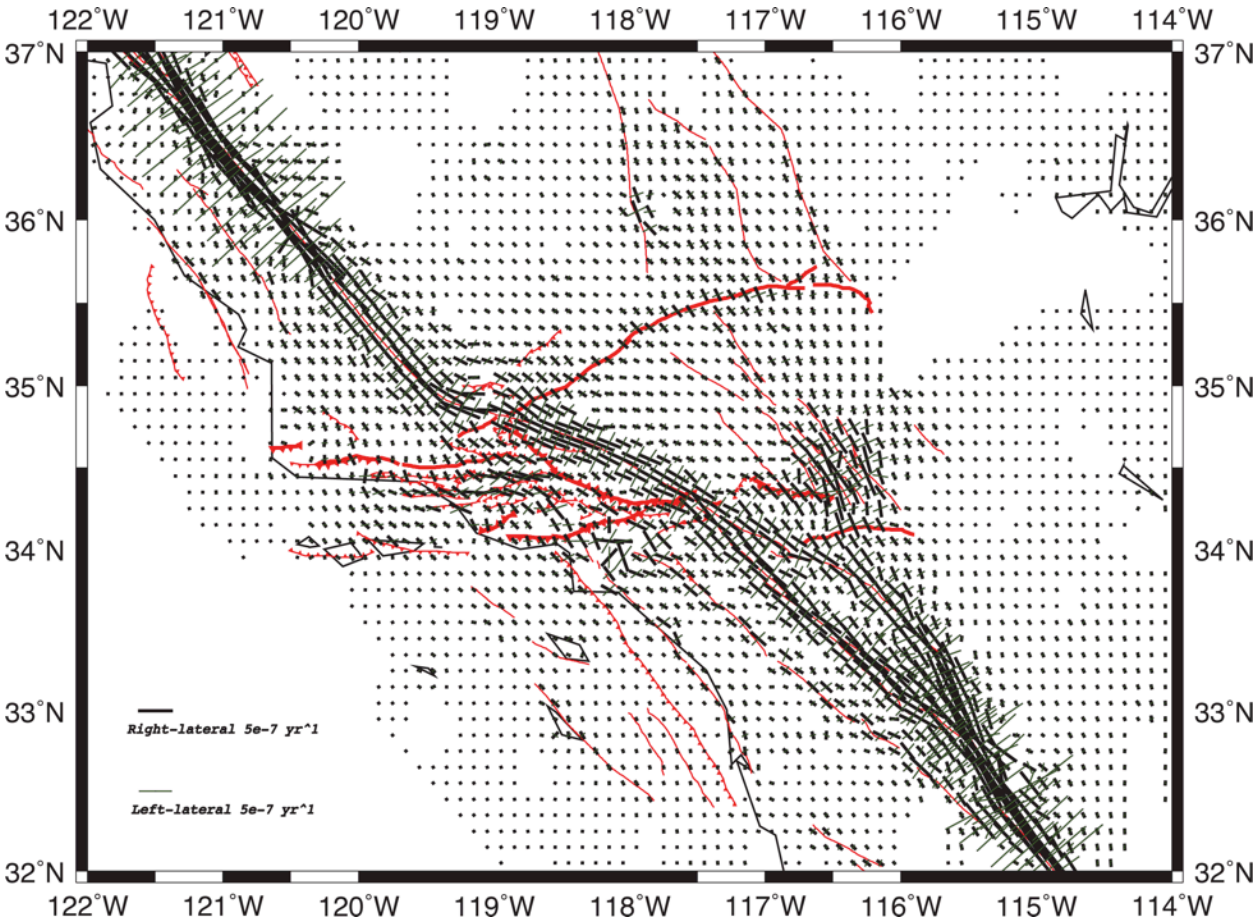

Figure 27. No-length-change directions. Orthogonal thick (right lateral) and thin (left lateral) bars indicate vertical strike slip faults. Parallel bars indicate normal or reverse faults. [*Holt,* 2014]

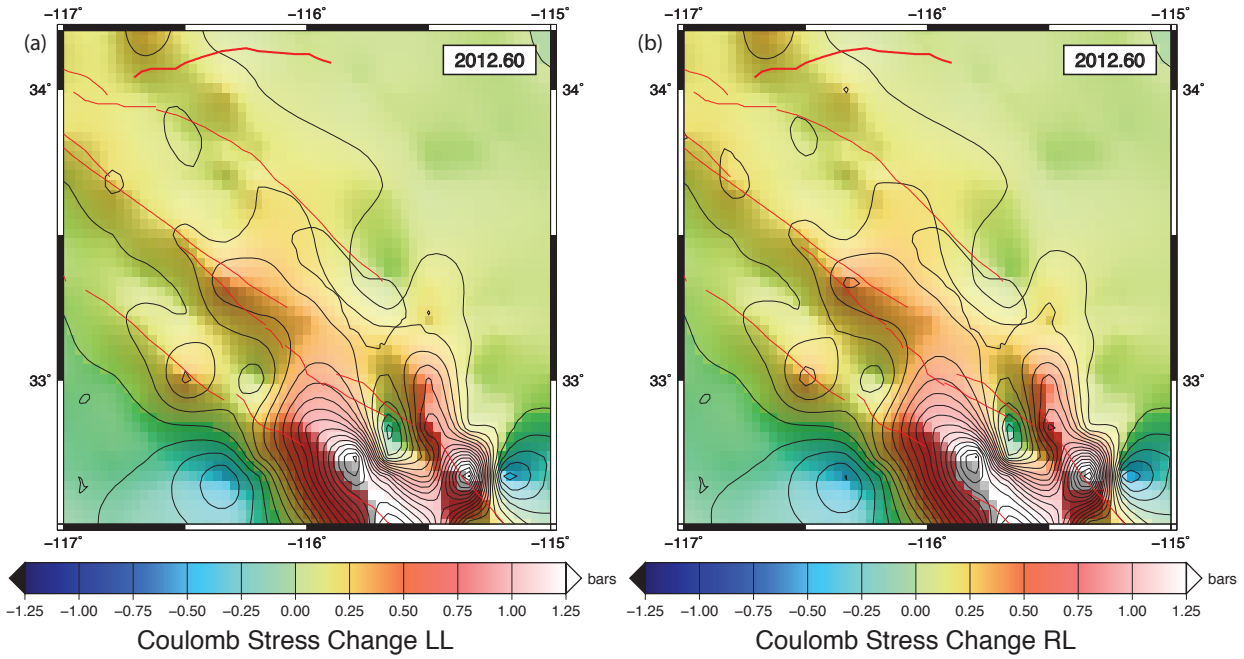

Figure 28. Total stress changes calculated using Equations 6, 7 & 8, from the total strain solutions spanning 4 April 2010 – 7 August 2012. Contour intervals of stress changes are 0.1 bars, μ' = 0.4. (**a**) Coulomb stress changes from a left lateral ψ. (**b**) Coulomb stress changes from a right lateral ψ.

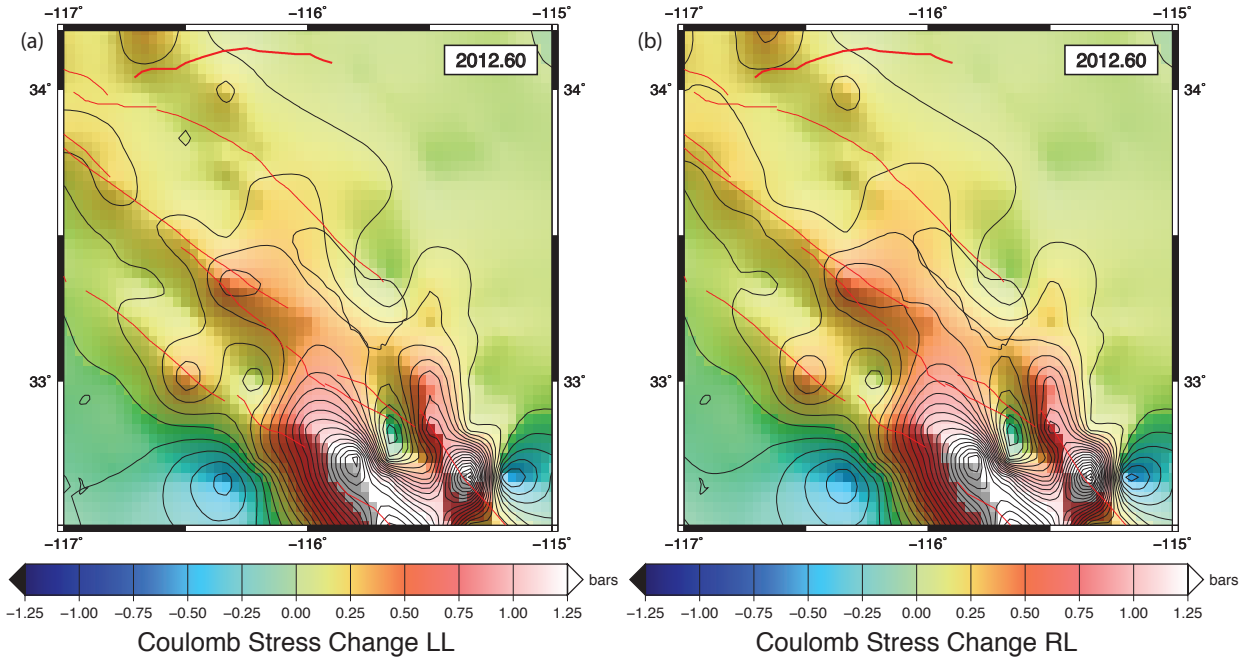

Figure 29. Total stress changes calculated using Equations 6, 7 & 8, from the total strain solutions spanning 4 April 2010 – 7 August 2012. Contour intervals of stress changes are 0.1 bars, μ' = 0.6. (**a**) Coulomb stress changes from a left lateral ψ. (**b**) Coulomb stress changes from a right lateral ψ.

4.3 - Coulomb Stress Change Results

The right lateral and left lateral stress changes were nearly identical for every solution (Figure 28, 29), indicating that the preferred fault planes are orthogonal, and the Southern San Andreas is a vertical strike slip fault. Although right lateral and left lateral Coulomb stress changes were calculated and modeled for all parameters (total, anomalous, with and without the coseismic, anisotropic and isotropic), I focused my analysis on the right lateral results since the right lateral no-length-change orientation (Figure 27) is consistent with the orientation of the San Andreas fault (Figures 30a-d, 31a-d, 32a-d, 33a-d & 34a-d.)

The lower Elsinore Fault immediately undergoes total stress loading after the El mayor event, with total stress accumulations beginning at 0.3 bars in April 2010, and it continues to load, reaching 0.5 bars by August 2012 (Figure 30a-d). The San Jacinto Fault experiences a positive total postseismic stress change up to 0.3 bars, which means it also continues to load for at least 2 years after the El Mayor event (Figure 30a-d). The Brawley Seismic Zone also experiences a steady rate of positive total stress changes post El Mayor, although they are smaller than the San Jacinto stress changes, peaking around 0.15 bars in August 2012. The total postseismic stress change solution shows a 0.1 bar negative stress change with each epoch along the southern San Andreas (closer to the Salton Sea), until the epoch ending in 2011.4, over a year after the event, after which the stress changes become positive there (Figure 30a-b). Loading then progresses steadily along the southern San Andreas, until the Coulomb stress changes peak at 0.2 bars in August 2012 (Figure 30c-d).

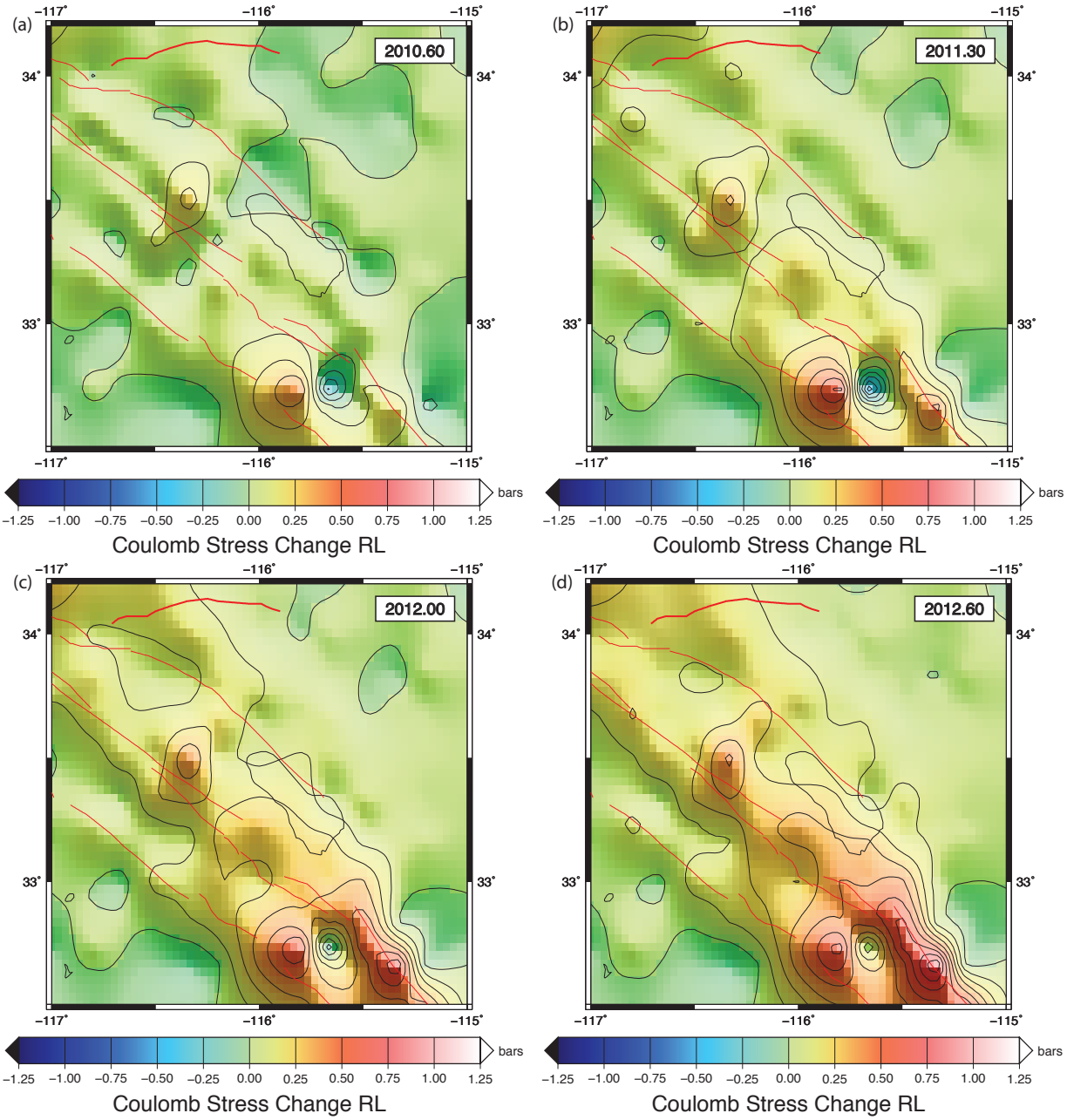

Figure 30. Total postseismic Coulomb stress change on right lateral vertical faults spanning (**a**) 5 April – 7 August 2010; (**b**) 5 April 2010 – 19 April 2011; (**c**) 5 April 2010 – 31 December 2011; (**d**) 5 April 2010 – 7 August 2012. Contour intervals of stress changes are 0.1 bars, μ' = 0.4.

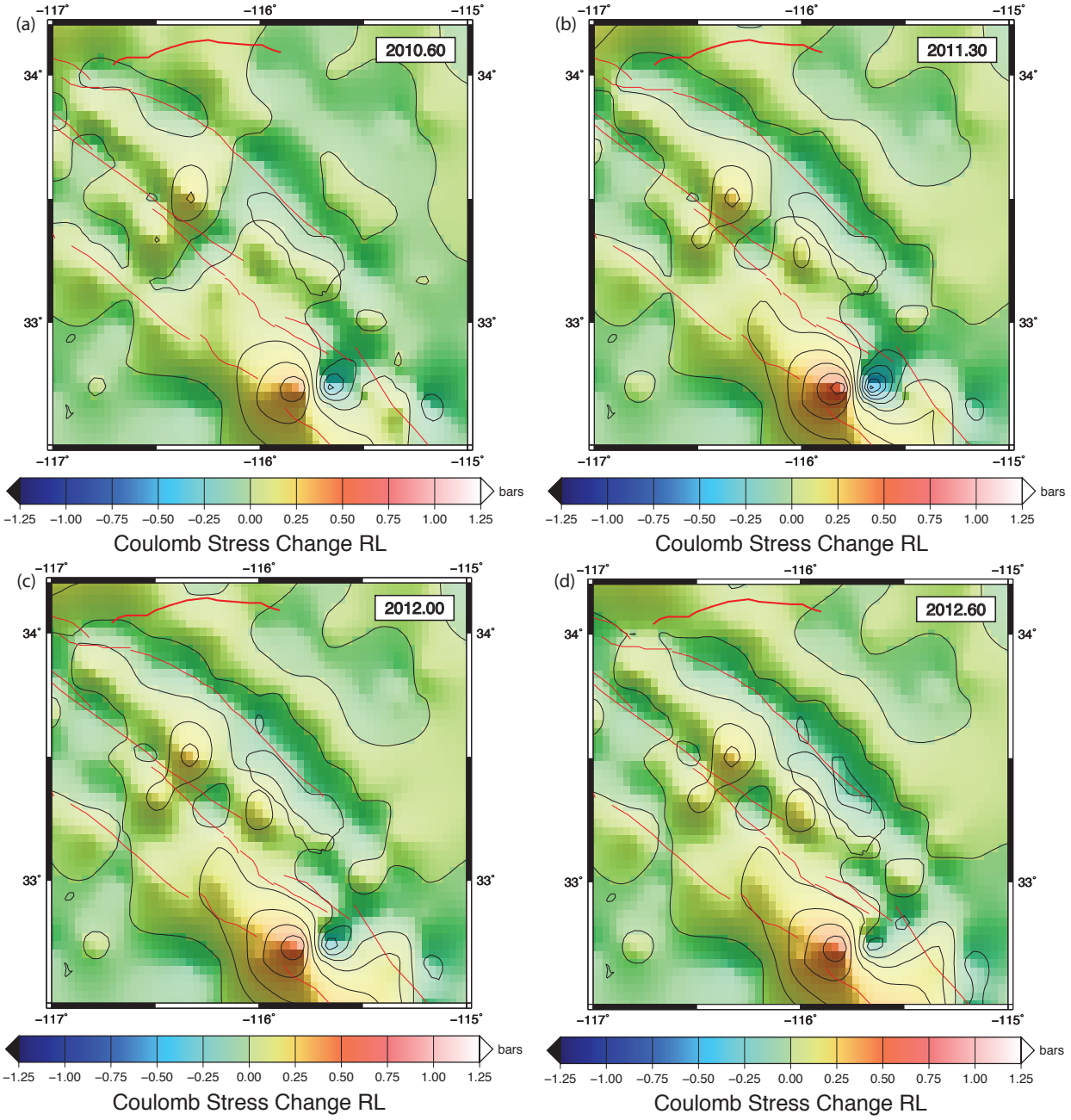

Figure 31. Anomalous postseismic Coulomb stress change on right lateral vertical faults spanning (**a**) 5 April – 7 August 2010; (**b**) 5 April 2010 – 19 April 2011; (**c**) 5 April 2010 – 31 December 2011; (**d**) 5 April 2010 – 7 August 2012. Contour intervals of stress changes are 0.1 bars, $\mu' = 0.4$.

Anomalous postseismic stress changes in the southern Elsinore Fault are nearly identical to the total postseismic stress changes here, which means that the postseismic El Mayor stress changes in this region were so large that they obscure any steady state loading (Figure 31a-d). The San Jacinto Fault has varying regions of small (+/- 0.05 bar) anomalous stress changes, and does not evolve much for the 2 years after the El Mayor event (Figure 31). The only notable feature is a "bulls-eye" of about 0.3 bars of Coulomb stress change, which does not evolve much over time (Figure 31). The southern San Andreas Fault experiences a steady anomalous negative Coulomb stress changes with time, around 0.1 bars (Figure 31a-d). A stagnant pocket of negative anomalous Coulomb stress change of approximately 0.1 bars occurs just West of the Brawley Seismic Zone (Figure 31a-d). However, the section of the Brawley Seismic Zone just north of the Imperial Fault undergoes a positive anomalous Coulomb stress accumulation of about 0.1 bars, which grows spatially over time (Figure 31a-d).

Total stress changes including the El Mayor coseismic perturbation are greater along the southern Elsinore Fault and in the Brawley Seismic Zone, when compared to total stress changes following the El Mayor event (Figure 30, 32). The southern Elsinore experiences 0.8 bars of loading from the coseismic onward (Figure 32a-d). The westernmost Brawley Seismic Zone actually undergoes a negative stress change of 0.5 bars, until May 2011, when total loading begins to increase (Figure 32a-b). From May 2011 through August 2012, the Brawley Seismic Zone experiences positive loading of up to 0.5 bars when the El Mayor coseismic stress changes are considered.

The major effect of the El Mayor coseismic stress signal on the anomalous stress evolution is that it creates a stagnant area of -0.4 – -0.3 bars of Coulomb stress change where the

southern San Jacinto meets the Imperial Fault (Figure 33a-d). The anomalous negative stress change here (coseismic plus postseismic), along the southern San Andreas Fault is slightly more negative (by approximately 0.1 bars) than the anomalous stress change without the El Mayor coseismic stress signal, particularly on the northeast side of the Salton Sea (Figure 31, 33).

The isotropic, homogeneous solution for anomalous stress changes is nearly identical to the anisotropic, inhomogeneous solution; it maintains the anomalous postseismic negative stress anomaly along the southern San Andreas and within the Brawley Seismic Zone, the near zero anomalous stress variability along the San Jacinto, and the larger positive stress changes on the southern Elsinore (Figure 34).

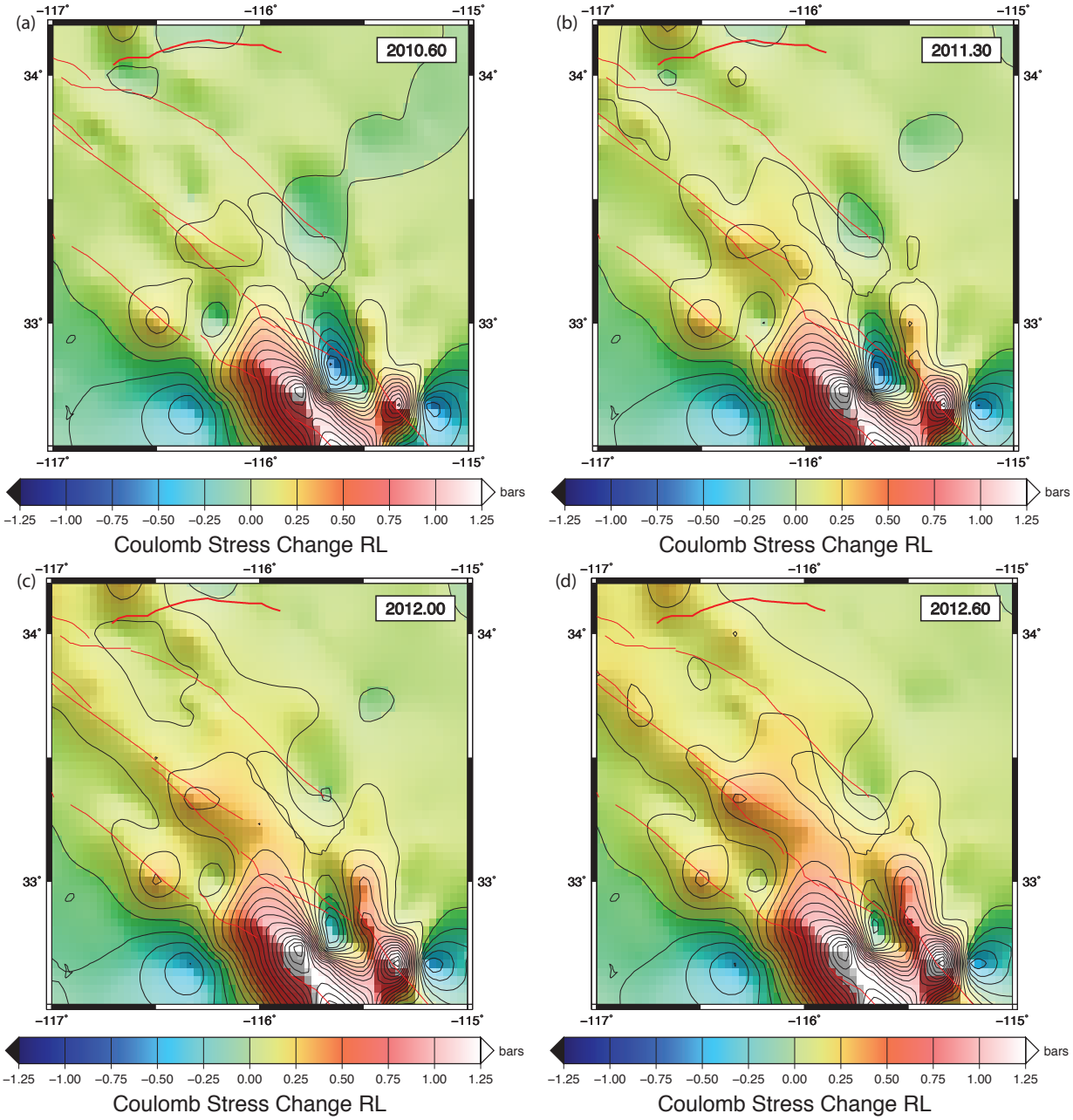

Figure 32. Total Coulomb stress changes on a right lateral fault with the coseismic stress perturbation included. Epochs represented are (**a**) 4 April – 7 August 2010; (**b**) 4 April 2010 – 19 April 2011; (**c**) 4 April 2010 – 31 December 2011; (**d**) 4 April 2010 – 7 August 2012. Contour intervals of stress changes are 0.1 bars, μ' = 0.4.

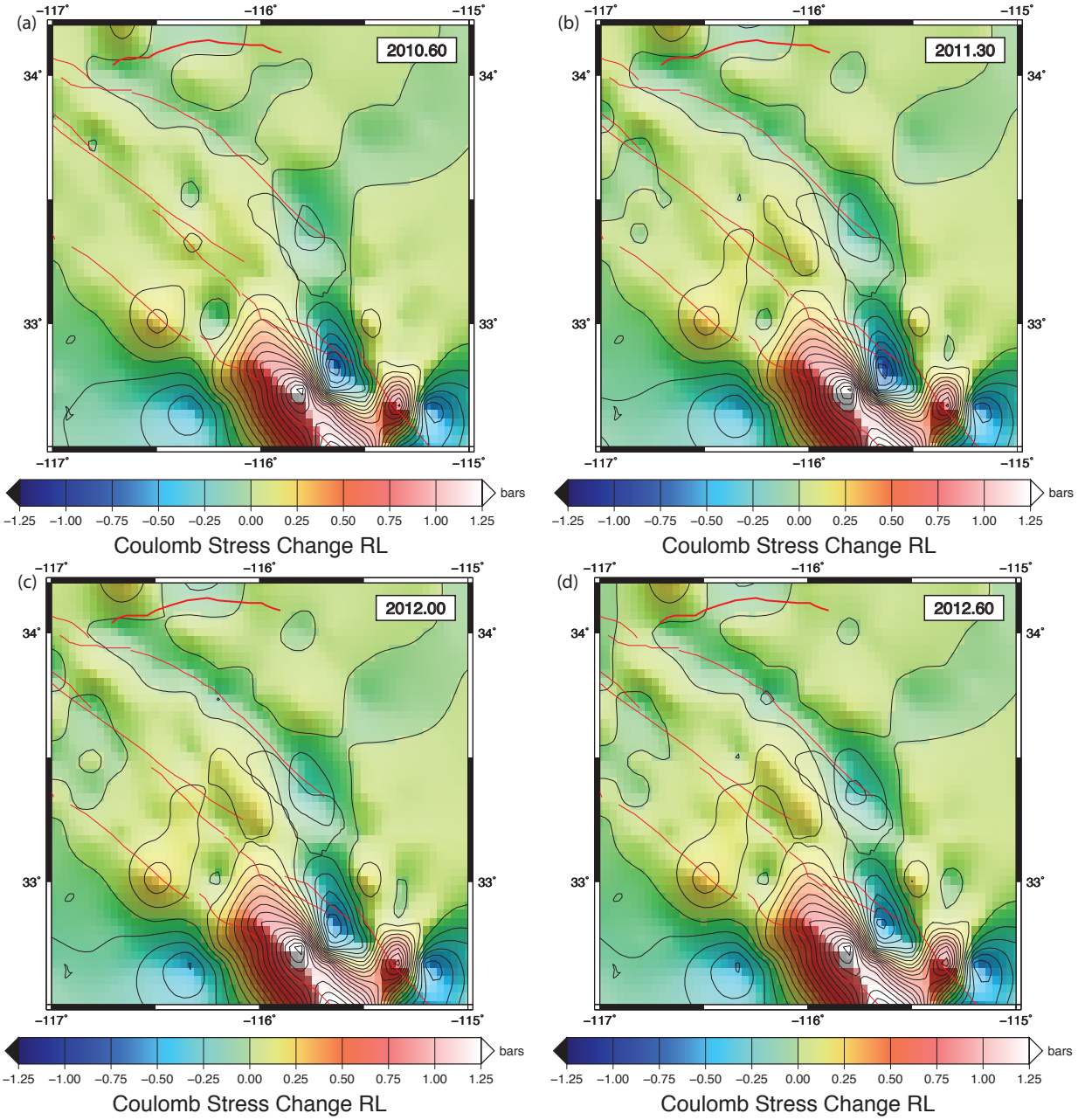

Figure 33. Anomalous Coulomb stress changes on a right lateral fault with the coseismic stress perturbation included. Epochs represented are (**a**) 4 April – 7 August 2010; (**b**) 4 April 2010 – 19 April 2011; (**c**) 4 April 2010 – 31 December 2011; (**d**) 4 April 2010 – 7 August 2012. Contour intervals of stress changes are 0.1 bars, μ' = 0.4.

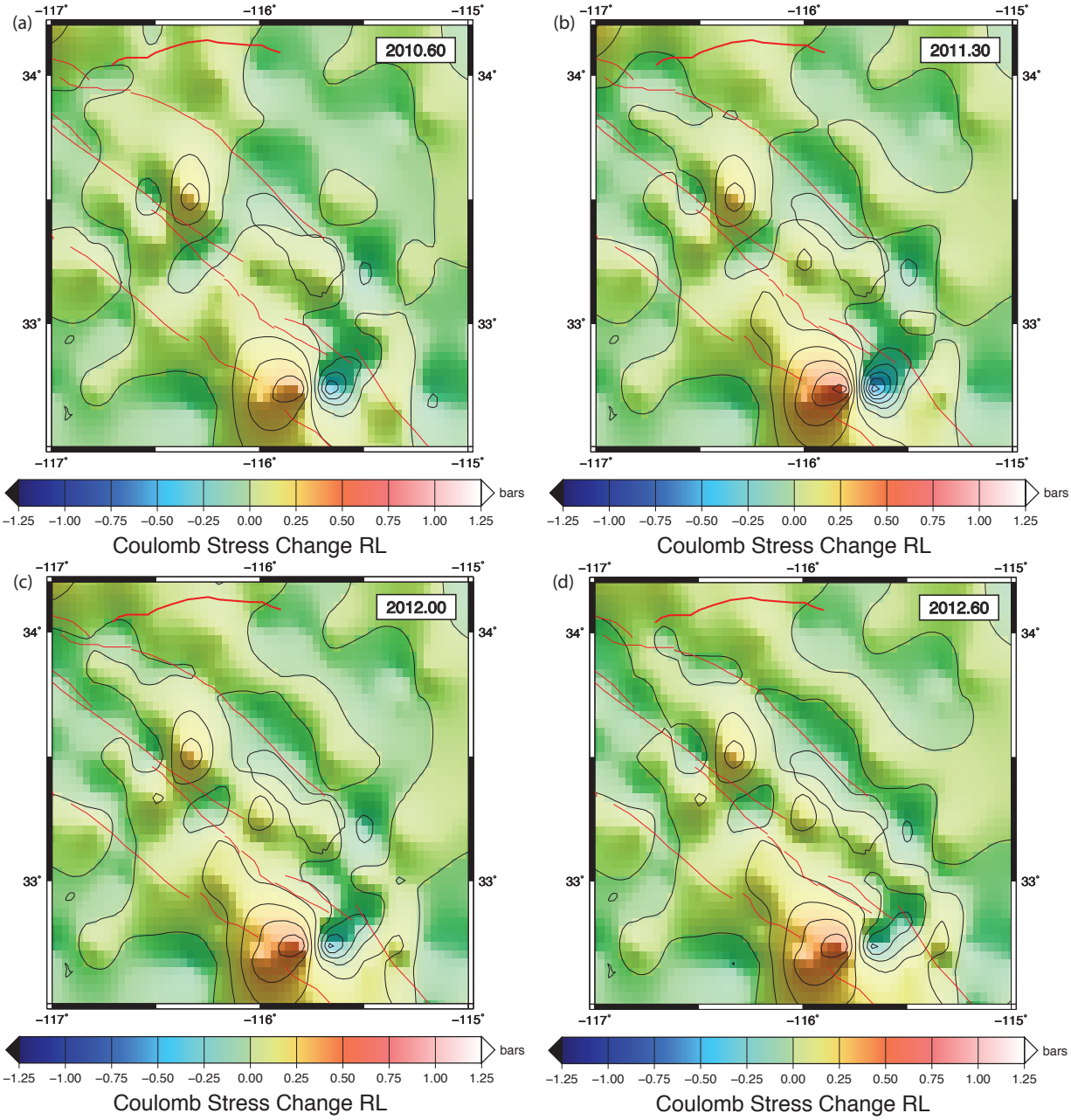

Figure 34. Anomalous postseismic Coulomb stress changes on a right lateral fault from an isotropic homogeneous solution, without the coseismic stress perturbation. The time epochs here are (**a**) 5 April – 7 August 2010; (**b**) 5 April 2010 – 19 April 2011; (**c**) 5 April 2010 – 31 December 2011; (**d**) 5 April 2010 – 7 August 2012. Contour intervals of stress changes are 0.1 bars, $\mu' = 0.4$.

4.4 – Discussion and Conclusions, El Mayor Postseismic Stress Evolution

The rate of loading along the San Jacinto Fault is relatively stable, because there is a nearly negligible anomalous stress change. This is consistent with the results from Chapter 3, which stated that the San Jacinto experiences a strain accumulation closely resembling the steady state.

Although total loading occurs throughout this region after the El Mayor event, a negative anomalous Coulomb stress change indicates that the rate of loading is less along the southern San Andreas and just to the West of the Brawley Seismic Zone (Figure 30, 31). That is, the difference from the steady state loading is negative, so loading occurs at a slower rate in these areas. The isotropic, homogeneous stress change results once again give credibility to the cGPS data and the anisotropic solution's propensity to place anomalies along fault zones. However, a future analysis of the pre-El Mayor regional stresses would determine whether or not this reduced rate of loading is a postseismic artifact. Additionally, including these stress rate changes in a rate/state model of with pre-El Mayor seismicity rates may increase our ability to forecast seismicity [*Toda et al.*, 2005; *Dietrich*, 1994]. Reduced rates of loading should result in lower seismicity rates [*Toda and Enescu*, 2011].

The El Mayor coseismic stress perturbation increased the total stress loading in the lower Elsinore Fault and the eastern Brawley Seismic Zone, decreased the stress loading rate in the western Brawley seismic zone and parts of the southernmost section of the San Andreas Fault, but left the San Jacinto relatively unaffected (compare Figure 30, 31 with Figure 32, 33). These coseismic stress effects are consistent with the modeled principal strain axes, which show a right-lateral strain orientation along the San Jacinto and a dominant N-S extensional strain

orientation along the southern San Andreas and surrounding regions (Figure 35). The coseismic appears to have aided the usual stressing regime on the San Jacinto and is consistent with the unclamping process of the southern San Andreas Fault.

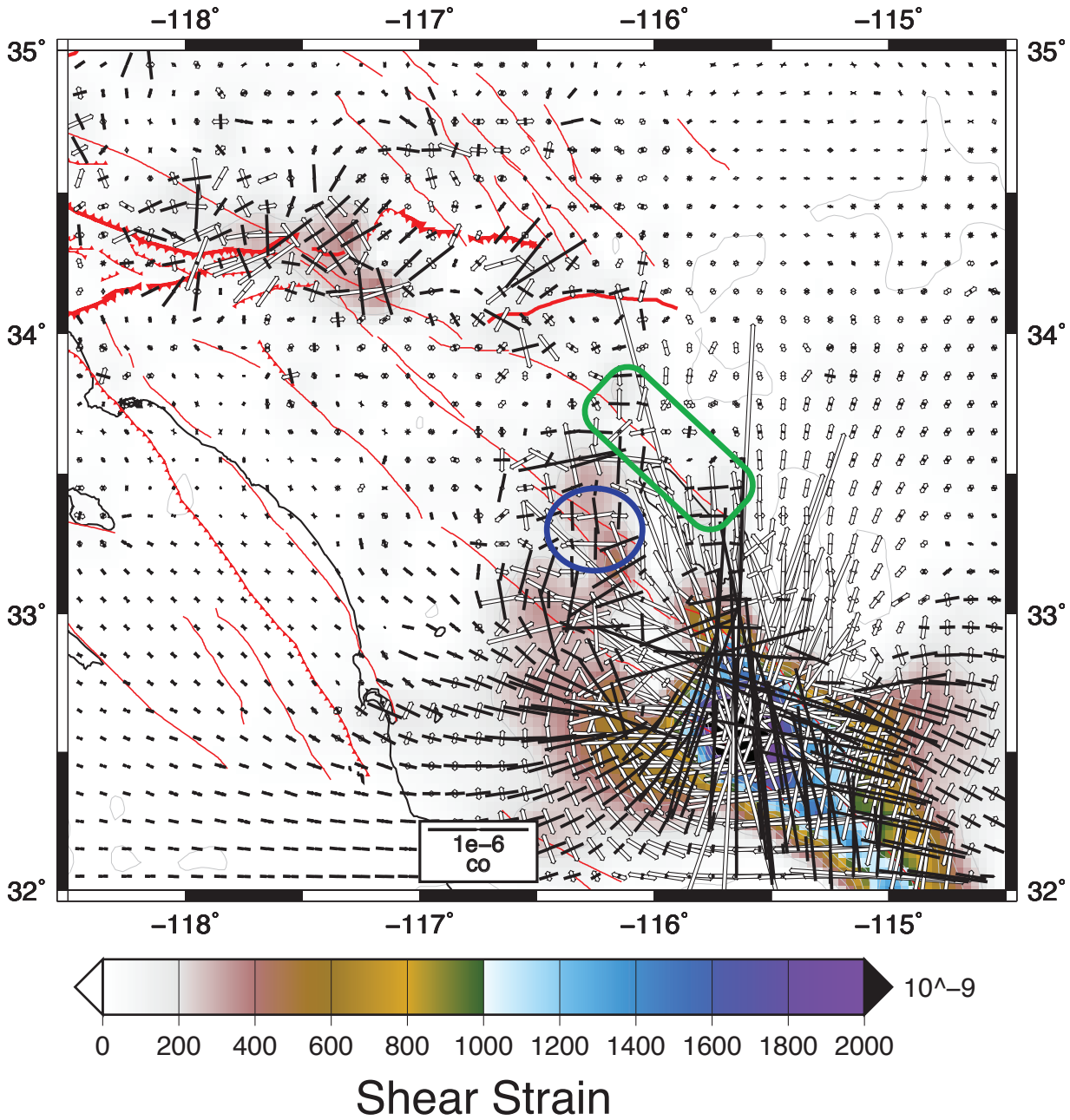

Figure 35. Principal strain axes for the one-day coseismic event on 4 April 2010, plotted over contoured shear strain. The blue ellipse highlights strain directions consistent with the steady strain state of the San Jacinto fault. The area circled in green shows extension north-south and compression east-west, opposite of the steady state of strain along the southern San Andreas.

The first 2 initial postseismic epochs, ps1 and ps2, experience the most dramatic surface deformation and relaxation (Figure 13b), so I sought to learn how this might be reflected in the total stress changes. I compared total postseismic stresses for all cumulative epochs with and without these additional strain results, for example, 2010.5-2010.9 + ps1 + ps2 compared with 2010.5-2010.9 (Figure 36a,b) and 2010.5-2012.6 + ps1 + ps2 compared with 2010.5-2012.6 (Figure 37a,b). The removal of the ps1 and ps2 total strains had an indistinguishable effect on total postseismic stresses on the southern San Andreas Fault, though they added some positive Coulomb stress changes to the San Jacinto and lower Elsinore faults. Therefore, the stress changes along the southern San Andreas Fault are influenced by more than immediate deformation and relaxation; the postseismic relaxation over the entire period is important.

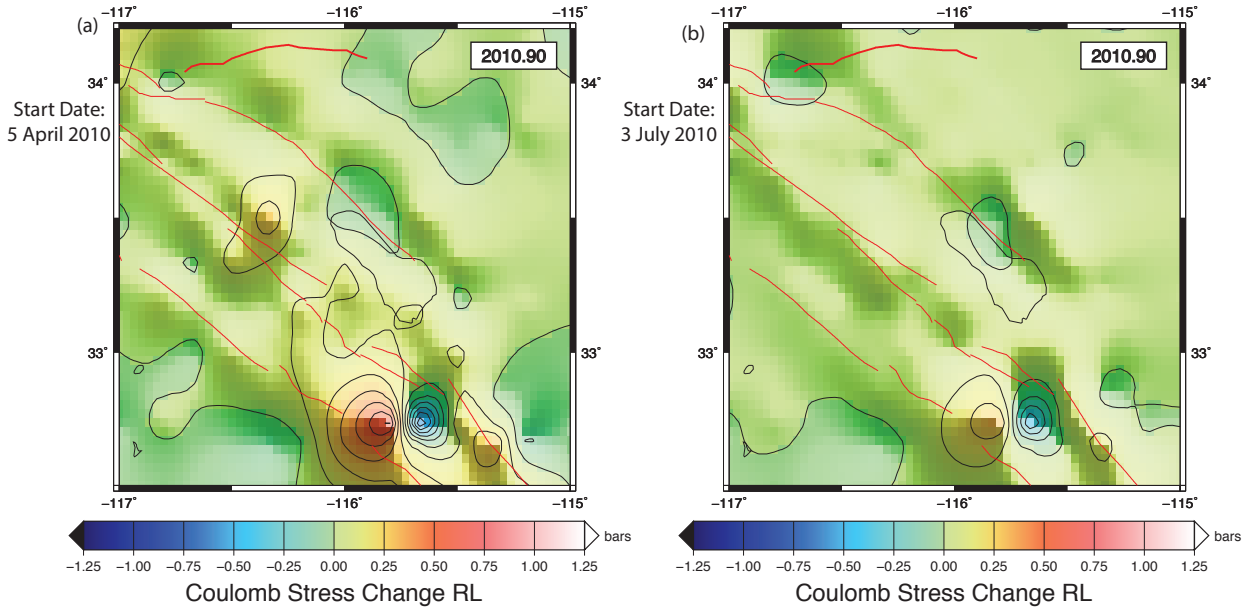

Figure 36. Total Coulomb stress changes for a right lateral fault over the periods (**a**) 5 April 2010 – 25 November 2010 and (**b**) 3 July 2010 – 25 November 2010. Contour intervals of stress changes are 0.1 bars, μ' = 0.4.

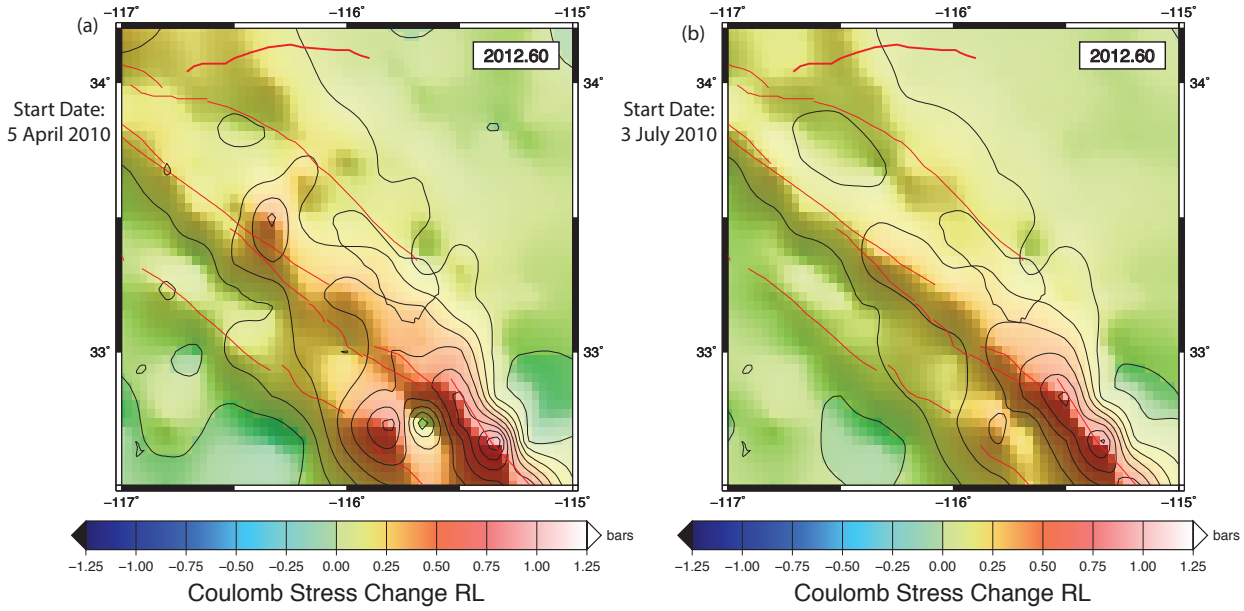

Figure 37. Total Coulomb stress changes for a right lateral fault spanning the periods (**a**) 5 April 2010 – 7 August 2012 and (**b**) 3 July 2010 – 7 August 2012. Contour intervals of stress changes are 0.1 bars, $\mu' = 0.4$.

Chapter 5 – Conclusions and Implications for Future Work

I helped develop a strain transient detection tool that had been previously tested on synthetic data and proven to be effective at locating areas of anomalous strain changes. Anomalous strains were detected in southern California over the 2.3 year period between the 4 April 2010 El Mayor-Cucapah earthquake and the August 2012 Brawley Swarm. This tool was then adapted to gain a better perspective on anomalous strains believed to be postseismic phenomena associated with the El Mayor event. This analysis lead to the discovery of unclamping along the southern San Andreas Fault, and extensional strains and strain rotations in the Brawley Seismic Zone. I used these discoveries to motivate a calculation of the Coulomb stress changes in this region. The Coulomb stress change analysis revealed a reduced rate of loading along the southern San Andreas and just West of the Brawley Seismic Zone. This may indicate a reduced seismicity rate in these regions and I recommend a future study of the Coulomb stress changes in a rate/state model that seeks to forecast seismicity, using the methods of *Dieterich* 1994 and *Toda et al.,* 2005.

References

Agnew, D. (2013), Realistic Simulations of Geodetic Network Data: The Fakenet Package, *Seis. Res. Lett.*, **84**, 419-425.

Bartlow, N. M., S. Miyazaki, A. M. Bradley, and P. Segall (2011), Space-time correlation of slip and tremor during the 2009 Cascadia slow slip event, Geophys. Res. Lett., 38, L18309, doi:10.1029/2011GL048714

Bawden, G. W. (2003), Separating ground-water and hydrocarbon pumping effects from tectonic contraction measurements across Metropolitan Los Angeles, CA, U.S. Geol. Surv. Open File Rep., 03-0308.

Baxter, S.C., Kedar, S., Parker, J.W., Webb, F.H., Owen, S.E., Sibthorpe, A., Dong, D.A. (2010) Limitations of strain estimation techniques from discrete deformation observations, *Geophys. Res. Lett*., **38**, doi: 10.1029/2010GL046028

Beavan, J; Haines, J, Contemporary horizontal velocity and strain rate fields of the Pacific-Australian plate boundary zone through New Zealand, *J. Geophys. Res*., **106**, p. 741-770, 2001.

Bird, P. (2009), Long-term fault slip rates, distributed deformation rates, and forecast of seismicity in the western United States from joint fitting of community geologic, geodetic, and stress direction data sets, *J. Geophys. Res.*, *114*, B11403, doi:10.1029/2009JB006317.

Crowell, B. W., Y. Bock, D. T. Sandwell, and Y. Fialko (2013), Geodetic investigation into the deformation of the Salton Trough, *J. Geophys. Res. Solid Earth*, 118, 5030–5039, doi:10.1002/jgrb.50347.

de Boor, A Practical Guide to Splines, Springer-Verlag, 1978.

Dieterich, James. "A Constitutive Law for Rate of Earthquake Production and Its Application to Earthquake Clustering." *Journal of Geophysical Research* 99.B2 (1994): 2601-2618

Dragert, H., and K. Wang (2011), Temporal evolution of an episodic tremor and slip event along the northern Cascadia margin, J. Geophys. Res., 116, B12406, doi:10.1029/2011JB008609

Dziewonski, A. M., T.-A. Chou and J. H. Woodhouse, Determination of earthquake source parameters from waveform data for studies of global and regional seismicity, *J. Geophys. Res.*, **86**, 2825-2852, 1981. doi:10.1029/JB086iB04p02825

Ekström, G., M. Nettles, and A. M. Dziewonski, The global CMT project 2004-2010: Centroid-moment tensors for 13,017 earthquakes, Phys. Earth Planet. Inter., 200-201, 1-9, 2012. doi:10.1016/j.pepi.2012.04.002

Freed, A. M. and R. Bürgmann, Evidence of power-law flow in the Mojave desert mantle, *Nature* **430**, 548, (2004).

Freed, AM; Bürgmann, R; Herring, T, Far-reaching transient motions after Mojave earthquakes require broad mantle flow beneath a strong crust, *Geophys. Res. Lett*., v. 34, doi: 10.1029/2007GL030959

Geng, J., Williams, S. D. P., Teferle, F. N. and Dodson, A. H. (2012), Detecting storm surge loading deformations around the southern North Sea using subdaily GPS, *Geophys. J. Int.* (2012) 191, 569–578 doi: 10.1111/j.1365-246X.2012.05656.x

Hauksson, E., W. Yang, and P.M. Shearer, "Waveform Relocated Earthquake Catalog for Southern California (1981 to 2011)"; *Bull. Seismol. Soc. Am.,* Vol. 102, No. 5, pp. –, October 2012, doi: 10.1785/0120120010

Hernandez, D., W. Holt, R.A. Bennett, C. Li, L. Dimitrova, and A.J. Haines (2005), Estimation of a time-dependent strain rate field in southern California using continuous GPS stations in the SCIGN network, *Eos Trans*. AGU, Fall Meet. Suppl., Abstract G43-A-05, 2005.

Hernandez, D., A methodology for quantifying the spatial and temporal coherence of velocity gradient tensor fields using CGPS data, M.S. Thesis, Stony Brook University, 2007.

Holt, W. E., and A. J. Haines (1993), Velocity fields in deforming Asia from the inversion of earthquake-released strains, Tectonics, 12*(*1*),* 1–20*, doi:*10.1029/92TC00658

Holt, W. E. and Ghosh, A. (2012), Using GPS Derived Shear Strain Rates in Southern California to Constrain Fault Slip Rate, Locking Depth, and Residual Off-Fault Strain Rates, presented at 2012 Fall Meeting, AGU, San Francisco, Calif., 3-7 Dec G22B-04.

Holt, W. E., and G. Shcherbenko. "Toward a Continuous Monitoring of the Horizontal Displacement Gradient Tensor Field in Southern California Using CGPS Observations from Plate Boundary Observatory (PBO)." *Seismological Research Letters* 84.3 (2013): 455-67.

Holt, W. E. (2014). 2014 SCEC Proposal: Quantifying Stress Changes on Faults Associated with Measured Geodetic Strains in Southern California. Southern California Earthquake Center.

Jennings, C. W., Fault activity map of California and adjacent areas, Cal. Dept. of Conserv., Div. of Mines and Geology, Sacramento, 1994.

Ji, K. H., and T. A. Herring (2011), Transient signal detection using GPS measurements: Transient inflation at Akutan volcano, Alaska, during early 2008, Geophys. Res. Lett., 38, L06307, doi:10.1029/2011GL046904.

King, G.C.P., R.S. Stein, and J. Lin, Static stress changes and the triggering of earthquakes, *Bull. Seismol. Soc. Amer.*, **84 (3),** 935-953, 1994.

King, N. E., et al. (2007), Space geodetic observation of expansion of the San Gabriel Valley, California, aquifer system, during heavy rainfall in winter 2004–2005, *J. Geophys. Res.*, 112, B03409, doi:10.1029/2006JB004448.

Larsen, S., and R. Reilinger, Age Constraints for the Present Fault Configuration in the Imperial Valley, California: Evidence for Northwestward Propagation of the Gulf of California Rift System, *J. Geophys. Res.*, **96 (B6)**, 10,399-10,346, 1991.

Lin, J., and R.S. Stein, Stress triggering in thrust and subduction earthquakes, and stress interaction between the southern San Andreas and nearby thrust and strike-slip faults, *J. Geophys. Res.*, **109**, B02303, doi:10.1029/2003JB002607, 2004.

Llenos, A. L., and J. J. McGuire (2011), Detecting aseismic strain transients from seismicity data, *J. Geophys. Res.*, **116**, B06305, doi:10.1029/2010JB007537

Lohman, R. B., and J. J. McGuire (2007), Earthquake swarms driven by aseismic creep in the Salton Trough, California, *J. Geophys. Res.,* **112**, B04405, doi:10.1029/2006JB004596

Luttrell, K. M., X. Tong, D. T. Sandwell, B. A. Brooks, and M. G. Bevis (2011), Estimates of stress drop and crustal tectonic stress from the 27 February 2010 Maule, Chile, earthquake: Implications for fault strength, *J. Geophys. Res.*, *116*, B11401, doi:10.1029/2011JB008509.

McGuire, J. J., and P. Segall (2003), Imaging of aseismic fault slip transients recorded by dense geodetic networks*, Geophys. J. Int.* (2003) **155,** 778–788.

Miyazaki, S., J. J. McGuire, and P. Segall (2011), Seismic and aseismic fault slip before and during the 2011 off the Pacific coast of Tohoku earthquake, Earth Planets Space, 63, 637–642, doi:10.5047/eps.2011.07.001.

Ohtani, R., J. J. McGuire, and P. Segall (2010), Network strain filter: A new tool for monitoring and detecting transient deformation signals in GPS arrays, J. Geophys. Res., 115, B12418, doi:10.1029/2010JB007442.

Okada, Y., Internal deformation due to shear and tensile faults in a half-space, *Bull. Seismol. Soc. Amer.*, **82 (2)**, 1018-1040, 1992.

Pollitz, F. F., R. Bürgmann, and W. Thatcher (2012), Illumination of rheological mantle heterogeneity by the M7.2 2010 El Mayor-Cucapah earthquake, Geochem. Geophys. Geosyst., 13, Q06002, doi:10.1029/2012GC004139.

Shen-Tu, B., W. E. Holt and A. J. Haines, The kinematics of the western United States estimated from Quaternary rates of slip and space geodetic data, *J. Geophys. Res,* ***104***, 28927-28955, 1999.

Shen, Z. - K., R. W. King, D. C. Agnew, M. Wang, T. A. Herring, D. Dong, and P. Fang (2011), A unified analysis of crustal motion in Southern California, 1970–2004: The SCEC crustal motion map, J. Geophys. Res., 116, B11402, doi:10.1029/2011JB008549

Smith, B., and D. Sandwell. "Coulomb Stress Accumulation along the San Andreas Fault System." *Journal of Geophysical Research* 108.B6 (2003).

Smith, B. R. and D. T. Sandwell (2006), A model of the earthquake cycle along the San Andreas Fault System for the past 1000 years, *J. Geophys. Res.*, *111*, B01405, doi:10.1029/2005JB003703.

Toda, Shinji, and Bogdan Enescu. "Rate/state Coulomb stress transfer model for the CSEP Japan seismicity forecast." *Earth Planets and Space* 63.3 (2011): 171.

Toda, S.*,* R. S. Stein*,* K. Richards-Dinger*, and* S. B. Bozkurt (2005), Forecasting the evolution of seismicity in southern California: Animations built on earthquake stress transfer*, J. Geophys. Res.,* **110***, B05S16, doi:*10.1029/2004JB003415.

Yang, W., E. Hauksson and P. M. Shearer, Computing a large refined catalog of focal mechanisms for southern California (1981 - 2010): Temporal Stability of the Style of Faulting, *Bull. Seismol. Soc. Am.*, June 2012, v. 102, p. 1179-1194, doi:10.1785/0120110311, 2012.

Appendix A: A Relevant Map of Southern California

I provide a map of the major faults in the area of Southern California and Northwestern Mexico to help guide readers unfamiliar with this region. The San Andreas Fault extends further north past San Francisco, but this thesis concentrates on its southernmost segment, which terminates at the Salton Sea (Figure 1A.) The San Jacinto, Elsinore, Laguna Salada and Imperial Faults are parallel to the San Andreas; the San Jacinto and Elsinore are west of the San Andreas, the Laguna Salada Fault is to the south of the Elsinore, and the Imperial Fault begins at the southernmost section of the San Jacinto Fault Zone (Figure 1A). The Brawley Seismic Zone is between the northernmost part of the Imperial Fault and the southernmost part of the San Andreas Fault. The location of the El Mayor-Cucapah event was 32.1°N and -115.3°W.

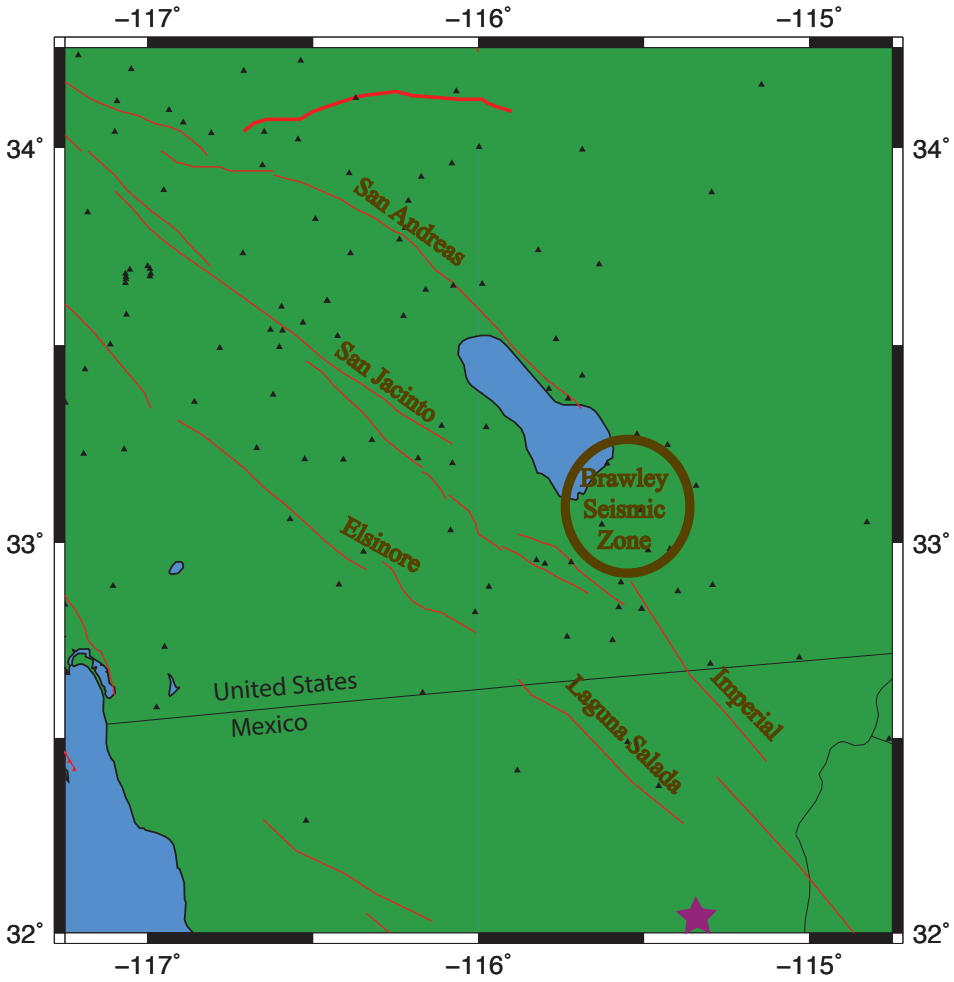

Figure A1. Map showing locations of the San Andreas, San Jacinto, Elsinore, Laguna Salada and Imperial Faults, as well as the Brawley Seismic Zone. The fuchsia star is the approximate location of the El Mayor event.